

This manuscript in post-review format was accepted for publication in International Journal of Engineering Science, and can be cited as follows

A. Ghazi, C. Tiago, P. Berke, B. Sonon, T.J. Massart, Efficient computational modelling of closed cell metallic foams using a morphologically controlled shell geometry, International Journal of Mechanical Sciences, 168, 2020, 105298

Efficient computational modelling of closed cell metallic foams using a morphologically controlled shell geometry

A. Ghazi^{a,b}, C. Tiago^b, B. Sonon^a, P. Berke^a, T.J. Massart^{a,*}

^a*Building, Architecture & Town Planning Department (BATir), Université libre de Bruxelles (ULB), CP 194/02, Avenue F.D. Roosevelt 50, 1050 Bruxelles, Belgium*

^b*CERIS, Instituto Superior Técnico, Universidade de Lisboa, Av. Rovisco Pais, 1049-001 Lisboa, Portugal*

Abstract

This contribution addresses the finite element modelling of closed cell metallic foams using Representative Volume Elements (RVEs) based on shell geometries directly extracted from implicitly defined 3D geometries. 3D RVEs of closed cell foam materials are produced by means of a generation strategy allowing a close morphological control reproducing fine scale geometrical features incorporating cell size, cell wall thickness and cell wall curvature distributions. The strategy is built on three computational ingredients: (i) a random packing algorithm based on random sequential addition assisted by neighbour distance control, (ii) a distance field-based shape tessellation (morphing) that allows incorporating cell wall curvatures and varying cell wall thicknesses and (iii) a close control on the shape of the cells. In order to decrease the computational cost of a full 3D finite element model, an original approach is proposed to produce a shell-based geometry directly from 3D information. Extracting the shell geometry from the implicitly defined 3D geometry based on the zero level of distance fields that would represent the cell walls is computationally impossible. Therefore, a novel robust procedure is proposed using careful cutting operations on distance fields for this purpose. The effect of the different microstructural geometrical features of interest on the average mechanical behaviour of the foam is investigated using shell-based finite element analyses. The computational cost and the accuracy of the proposed shell models are then assessed by comparing their results to full 3D simulations. The macroscopic behaviour of the generated shell-based model under compressive loading is then assessed up to the densification stage (including contact), and compared qualitatively with experiments from the literature. The macroscopic behaviour of the shell-based model is explained by linking it to cell/wall level deformation mechanisms.

Keywords: Closed-cell metallic foam, Shell geometry, Finite elements, RVE generation, Computational Homogenization, Morphological control

*Corresponding author.

Phone: +32 26502742, Fax: +32 26502789

thmassar@ulb.ac.be (T. J. Massart)

URL: <https://batir.ulb.ac.be/index.php> (T. J. Massart),

1. Introduction

Closed cell metallic foams are increasingly used in many industrial applications, because of their interesting features such as low density, high energy absorption and high strength to weight ratio. Closed cell foams are geometrically complex and their microstructure can be described using various statistical indicators such as cell size distribution, cell wall thickness distribution, cell wall curvature, number of faces per cell, number of edges per faces, *etc.* Variations in such microstructural features were shown to affect their mechanical behaviour [1].

When observed at the macroscopic scale, closed cell foams response under compression can be split in three consecutive strain regimes. An initial linear elastic domain is followed by a plateau at a practically constant macroscopic stress level, followed by a third strain range also called densification, in which the foam is compacted [2].

The base material properties [3], relative density [4, 5] and geometrical features [2, 6, 7, 1] are known to affect the mechanical behaviour of closed cell foams with different magnitudes of influence. Nevertheless, the effect of individual features of the microstructure on the macroscopic mechanical response was not yet fully quantified. Therefore the investigation of these effects is useful to provide more insight both from an engineering perspective and also for helping manufacturers to improve the produced foams.

Many authors investigated the effect of the microstructure on the compressive response of foams experimentally [8, 9, 10, 2, 11, 12]. Due to the complexity of the manufacturing methods and of experimental tests, investigating the influence of each morphological parameter separately is not possible. A dedicated computational methodology incorporating detailed morphological features in a controllable way can be useful in this aspect. Another main advantage of such numerical models defined at the micro scale is that the link between the micro scale deformation mechanisms of the cells and the macro scale average mechanical behaviour can be naturally investigated.

Numerical microstructural approaches for closed cell foams can be categorized in three groups: (i) space filling polyhedron models [13, 14, 15, 16, 17, 18], (ii) image based models [19, 12, 20] and (iii) tessellation based models [21, 22, 23, 24, 25, 26, 27, 28, 29]. Space filling polyhedron models can be easily constructed and then be analyzed using shell finite element because they radically simplify the foam geometry. X-ray computed tomography (CT) provides more accurate information about the foams sample, however the findings validity is often limited to the studied sample and it does not allow investigating the individual effect of microstructural features. Either Voronoi and Laguerre tessellation based models can also be discretized with computationally efficient shell finite elements, but they can incorporate only a limited set of microstructural features and their variability.

Many researchers used tessellation-based models for closed cell foams to consider probabilistic geometrical features in combination with shell-based finite element analysis on the microstructural scale [22, 25, 27, 26, 30, 24]. For instance, [27] studied the effect of cell size variation on the elastic stiffness of closed foams and observed that the

foam stiffness is decreased by increasing the cell size variation. [26] showed that increasing the cell size and cell wall thickness variations results in a lower macroscopic Young's modulus. [21] also observed that the cell size dispersion influences the Young's modulus significantly. They also mentioned that, due to the lack of details of microstructural features in their tessellation-based models, the obtained results overestimate experimental data in terms of stiffness.

Some of the metallic foam morphological features (*i.e.* cell wall curvature with wriggles and corrugations, plateau borders) are usually lacking in most computational contributions. In a previous work [31], a methodology was developed to generate 3D foam geometries complying with real probabilistic foam data which naturally incorporates spatial thickness variations in the cell walls, as well as the plateau borders at the wall edges. Even though such 3D finite element models allow investigating the effect of microstructural features, they were observed to be computationally expensive, even when restricted to a loading of 5% macro strain and without considering contact conditions. This motivates the current proposal of a shell-based modeling strategy starting directly from this 3D data, with a *computation cost in the finite element analysis reduced by 2 orders of magnitude and offering a reasonably good accuracy.*

This contribution presents an original methodology, which allows generating and discretizing automatically a surface geometry starting from an implicitly defined 3D geometry for closed cell foam RVEs, while preserving all microstructural features of interest: cell size, cell wall curvature, cell wall thickness distributions, number of faces per cell and number of edges per face. Each step of the implemented approach is presented: from the close packing algorithm, through the deduced 3D implicit geometry, to the extraction of a surface/shell geometry and with its finite element meshing. The resulting tool is then used to simulate the compression of a closed cell foam RVE, incorporating various morphological features and their variation. The individual influence of these features on the mechanical response of the foam under compression is investigated and the shell model accuracy is quantified by critically comparing the obtained results to those of full 3D continuum finite element models for the same cell spatial organization. Another novel contribution is the computational study of compression loading of a RVE up to densification by taking contact into account and the qualitative comparison of computation results to experimental data from the literature.

This contribution is structured as follows. In Section 2, the methodology to generate 3D RVEs by morphing a set of arbitrary shaped inclusions is briefly recalled and the procedure to control and impose the relevant morphological features is outlined. Then the focus is set on the extraction algorithm of the surface geometry starting from the 3D implicit geometry, as well as on the surface meshing to create robust shell finite element models. The flexibility of the proposed methodology is illustrated by means of a parametric study of the effect of relevant microstructural features in Section 3. This is followed by a discussion on the performance of shell models versus 3D models, with a special focus on accuracy and computational cost in Section 4. The ability of the shell model to reproduce experimental results in a full compression test is demonstrated in Section 5, followed by the conclusions and perspectives in Section 6.

2. Morphologically sound shell finite element modelling of closed cell metallic foams

The simulation of the mechanical behaviour of a closed cell metallic foam with a 3D finite element model under compression loading was shown to be very expensive computationally due to the large number of degrees of freedom (DOFs) induced by the complex geometry [31]. Among the available solutions to reduce this computation cost (*e.g.* domain decomposition methods), one possible approach is to use shell finite elements because cell faces of closed cell foams comply with shell assumptions *i.e.*, the ratio of thickness to the spans of cell walls is appropriate.

A closed cell 3D geometry can be defined implicitly with level sets functions as shown in [32] and exploited using 3D volumetric finite elements in [31]. The missing ingredients for a successful shell-based finite element modelling with respect to these earlier efforts is a robust procedure for the extraction of a surface geometry from this 3D data with a special care to preserving the embedded morphological features. This section is dedicated to such a numerical procedure as an original contribution. An overview of the generation procedure to obtain the 3D implicit RVE geometry is first given, being a preliminary step to the surface geometry extraction. The proposed procedure for shell geometries is elaborated step by step to extract the surface geometry from the 3D implicit geometry of the closed cell foam.

2.1. 3D implicit geometry generation for closed cell metallic foam RVE

For the sake of completeness, the main steps of the generation of a 3D implicit geometry for a closed cell foam with microstructural morphological control are recalled here, see [31]. Complex geometries, such as closed cell foams, can be described in an implicit framework by using a combination of level set functions and signed distance fields [32]. In the present contribution, level set functions and signed distance fields are evaluated through a discrete set of data sampled on a regular grid (see Fig 1). Any level of those functions can also be extracted and represents then an explicit geometry. It then consists of a contour (2D) or a triangulated surface (3D) obtained by using a contouring method, such as the marching cube approach.

A signed distance function to a closed surface $DS_i(\mathbf{x})$, *e.g.*, an inclusion/cell (ϕ_i), divides the domain into two subdomains, where the distance from grid points (\mathbf{x}) to the surface is negative inside the inclusion, Ω_i^- or positive outside the inclusion, Ω_i^+ , respectively. The zero level set of the $DS_i(\mathbf{x})$ function, which describes inclusion i explicitly, can be extracted from this implicit information, as shown in Fig 1. Due to the finite accuracy of the implicit description of the geometry and of the employed interpolation scheme, the extracted explicit geometries are smooth and do not exhibit sharp edges. The presence of sharp geometrical features, such as at cell wall junctions in a shell description, requires special care for its conformal meshing [33].

The 3D implicit geometry generation methodology consists of three main computational steps:

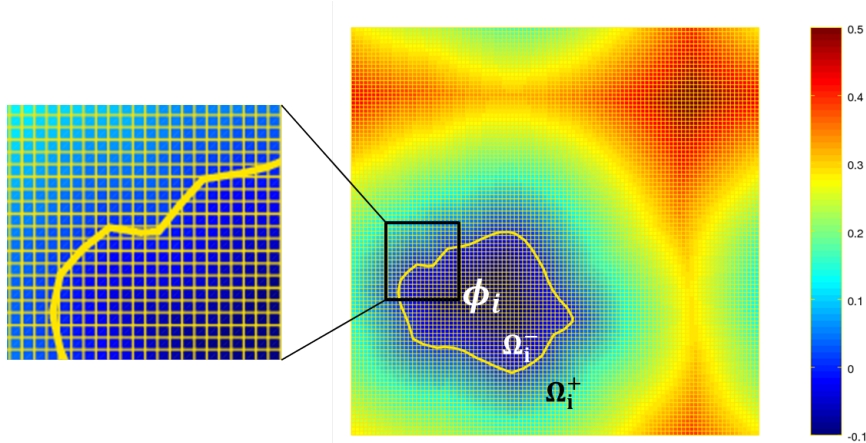


Figure 1: A 2D illustration of a periodic signed distance field for an inclusion ϕ_i as well as its zero level set contour that is obtained by the contouring of a discrete set of data sampled on a 2D regular grid.

- A level set-assisted random close packing algorithm based on a random sequential addition (DN-RSA) [34]
- A distance field-based shape tessellation (morphing) [32]
- A microstructural feature control procedure [31].

A recently developed mesh generation technique for heterogeneous microstructures represented by implicit functions [35, 36] is employed to mesh the generated implicitly defined RVE geometry for further 3D finite element analysis.

The DN-RSA packing algorithm is itself structured in three main steps: (i) the generation of inclusions based on an input cell size distribution in which an appropriate noise value is introduced on the inclusion shape to get the desired wall curvature, (ii) a random spatial dispersion of inclusions by using a distance field-based non-overlapping criterion to prevent inclusions inter-penetrations and (iii) the packing of the produced arbitrary shaped inclusions assisted by the knowledge of distances to previously added inclusions.

The local signed distance function $DS_i(\mathbf{x})$ is computed during the packing process for each added inclusion i . Global neighbour distance functions $DN_k(\mathbf{x})$ can also be defined for closed cell foam descriptions, where $DN_{k=1,2}$ is the k^{th} neighbour distance field to the k^{th} neighboring inclusion. It gives at every grid point \mathbf{x} of the domain, the distance to the k^{th} nearest inclusion. For instance, $DN_1(\mathbf{x})$, a global level set function representing all the inclusions in the packing, is computed as $DN_1(\mathbf{x}) = \min_i(DS_i(\mathbf{x}))$. It is worth mentioning that the signed distance fields $DS_i(\mathbf{x})$, in addition to the level set functions properties, satisfy the Eikonal equation $|\nabla(DS_i(\mathbf{x}))| = 1$, which will be mentioned in Section 2.2.2. The first and second neighbour distance fields (denoted as $DN_1(\mathbf{x})$, $DN_2(\mathbf{x})$) are also computed during the packing process.

These level set functions can be exploited to construct the 3D closed cell foam geometry using a morphing step.

A closed cell foam geometry is indeed defined with a constant minimal thickness of the wall $2t$, using a Voronoi-like level set function defined as:

$$O_V(\mathbf{x}) = DN_2(\mathbf{x}) - DN_1(\mathbf{x}) - t. \quad (1)$$

An example of a packing of inclusions and of their morphing is given in Fig 2.

For the sake of illustration of this generic methodology, morphological indicators, *i.e.* cell wall curvature, cell wall thickness and cell size distribution are controlled to comply with experimental data from the literature for ALPORAS closed cell foams [8, 37, 10, 11] in this contribution. Some features are controlled *a priori* as raw input data: such as the cell size distribution, the cell wall thickness distribution and the cell wall curvatures, based on a noise added to spherical inclusion shape. Other microstructural features of the foam, *i.e.* number of faces per cell and number of edges per face are verified *a posteriori*, see [31]. The shell modelling approach is based on a geometry obtained from this 3D implicitly defined closed cell foam geometry described by individual $DS_i(\mathbf{x})$ functions for each inclusion i . From now on, the term “cell” will be used. It refers to the foam cells obtained by the morphing procedure and is now pointed by indexes and exponents. The extraction and discretization procedure of the surface geometry from the used level set functions is elaborated in the next subsections.

It should be noted that the implicit and explicit representations of the geometry are used interactively in the proposed approach. The following notations of $O_{V_{ij}}$ (implicit geometry), $MS_{O_{V_{ij}}}$, $F_{MS_{ij}}$ and $E_{F_{ij}}^k$ (explicit geometry) are introduced in this paper for the sake of clarity. $O_{V_{ij}}$ refers to the level set function which is implicitly describing the mid surface between cells ϕ_i and ϕ_j , computed as

$$O_{V_{ij}}(\mathbf{x}) = DS_i(\mathbf{x}) - DS_j(\mathbf{x}). \quad (2)$$

It is emphasized that $O_{V_{ij}}$ deduced from local distance field functions $DS_i(\mathbf{x})$, is different from the O_V function deduced in equation (1) from the global distance fields DN_k . $MS_{O_{V_{ij}}}$ refers to the triangulated mid surface (explicit geometry) between cells ϕ_i and ϕ_j which is extracted from level set function $O_{V_{ij}}$ by contouring. $MS_{O_{V_{ij}}}$ is evolving during the cutting operations to approach $F_{MS_{ij}}$, the aimed cell face located between ϕ_i and ϕ_j . $F_{MS_{ij}}$ is obtained by successive cutting operations of the associated triangulated mid surface $MS_{O_{V_{ij}}}$ by gradually taking the presence of other cells (ϕ_k) into account. Finally $E_{F_{ij}}^k$ refers to an edge belonging to face $F_{MS_{ij}}$ which is cut by cell k (see Fig 3). Each face $F_{MS_{ij}}$, consists of edge points $E_{F_{ij}}^k$, corner points (points shared by two edges) and the points on the face.

Another set of junction points (representing the true position of junctions) and a set of frame points (representing the true position of faces connecting points) is also constructed subsequently, as will be explained in Section 2.2.2. The combination of these points after a smoothening step forms the initial set of points that are introduced in the

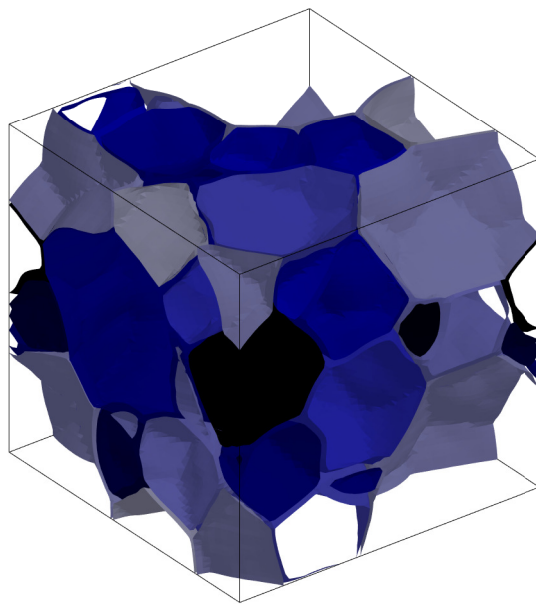
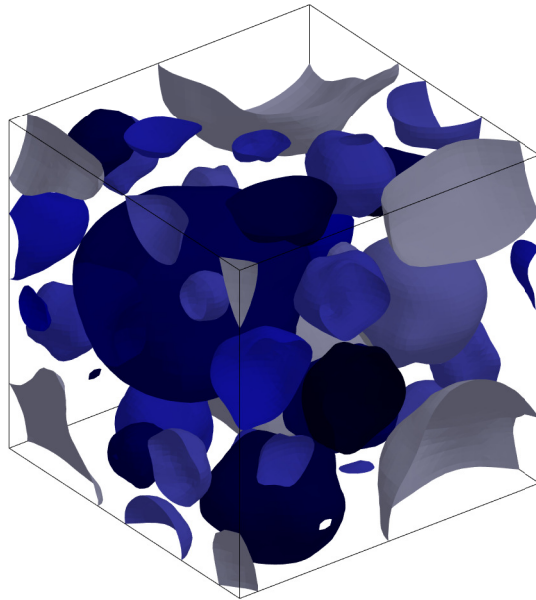


Figure 2: An example of inclusions packing (top) with morphing of these inclusions (bottom) obtained from the morphology controlling procedure [31]

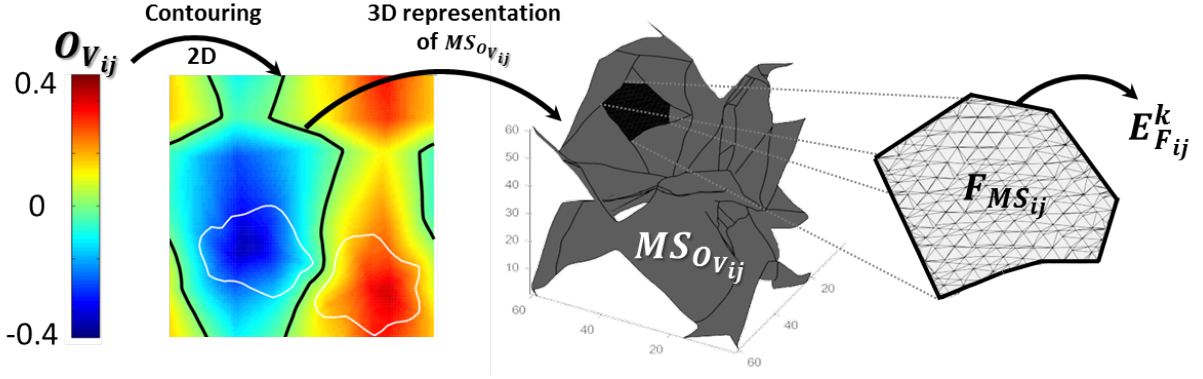


Figure 3: Illustration of the introduced notations of $O_{V_{ij}}$ (level set function which is implicitly describing the mid surface), $MS_{O_{V_{ij}}}$ (triangulated mid surface), $F_{MS_{ij}}$ (the aimed cell face) and $E_{F_{ij}}^k$ (an edge belonging to the aimed cell face) between cells i and j .

surface meshing tool and eventually become shell finite element mesh nodes.

2.2. Surface (shell) finite elements mesh construction

The signed distance field $DS_i(\mathbf{x})$ for each cell has been produced during the morphing operations and is readily available. This information is shown to be necessary and sufficient to construct the surface (shell) geometry. The proposed global procedure for obtaining a shell finite element mesh is illustrated in Fig 4 and is presented below according to the work flow of the implementation with the following steps: (1) discrete cell faces extraction; (2) meshing of the frames and construction of an open foam-like structure; (3) point cloud smoothening; (4) surface meshing (reconstruction); (5) surface mesh post processing.

2.2.1. Discrete cell faces extraction

Each cell in the 3D closed cell foam geometry is bounded by many faces that separate the cells from each other. These faces can be defined mathematically by using the Voronoi-like level set function $O_{V_{ij}}$ restricted to two cells i and j (Equation (2)). However, taking exactly the zero level set of this function in order to extract a surface geometry with zero thickness is impossible computationally due to the resolution of the discrete grid used in the 3D domain. It is therefore required to perform careful cutting operations on the generated 3D geometry with controlled fine scale features in order to obtain the corresponding surface geometry. The objective is to properly extract the faces ($F_{MS_{ij}}$) between each pair of cells ϕ_i and ϕ_j bounded by other cell faces based on the level sets information $O_{V_{ij}}$ and $O_{V_{ik}}$ (with $k \neq \{i, j\}$ and $\{i, j, k\} \in n$, n being the total number of cells), by using the individual signed distance function $DS_i(\mathbf{x})$ attached to each cell.

To illustrate the surface geometry extraction procedure, a 2D representation of the problem is considered in Fig 5 for the sake of simplicity and visibility. Each cell face between two cells i and j ($F_{MS_{ij}}$) can be built separately. It

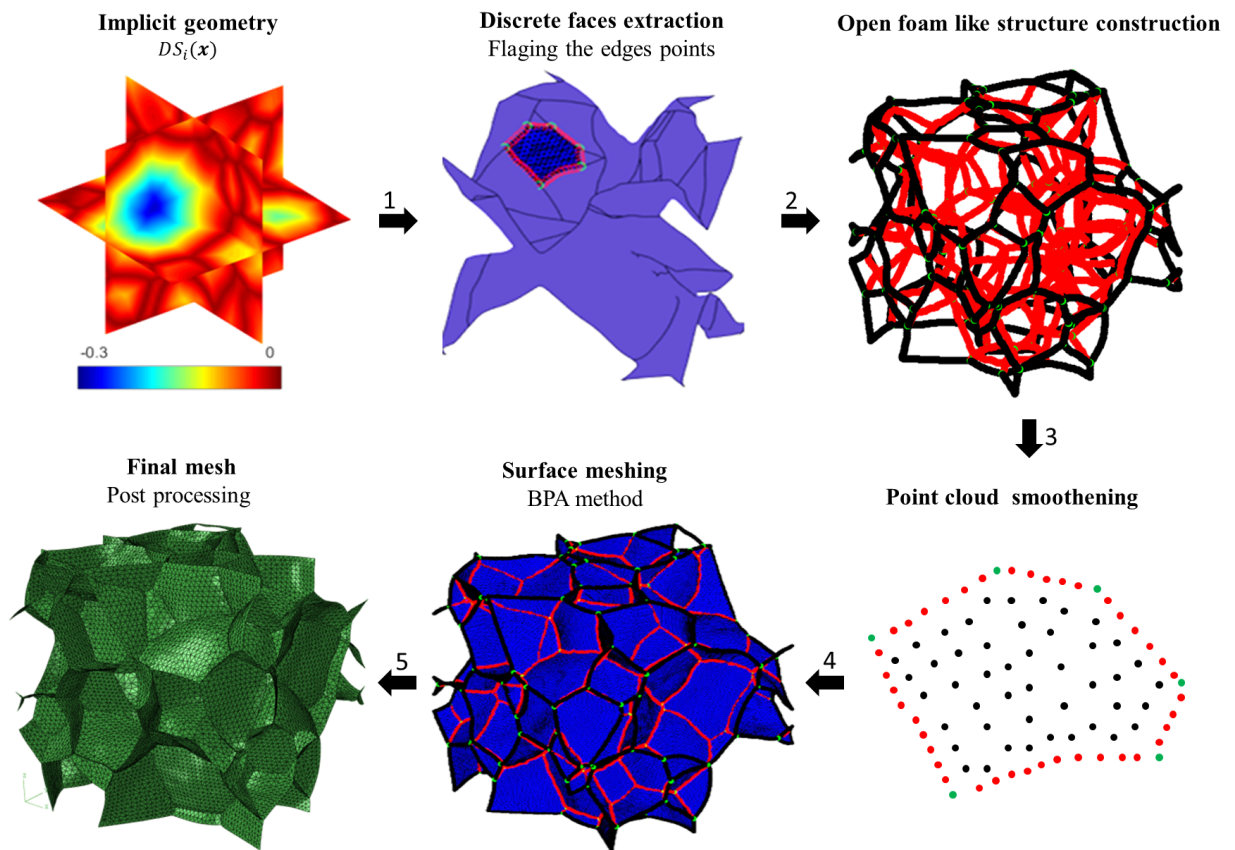


Figure 4: Global procedure for the meshing and surface extraction process divided in 5 steps taking the 3D implicit geometry as input.

is the remaining part of the mid surface ($MS_{O_{V_{ij}}}$) of these cells after cutting it by the adjacent cell walls with which they share an edge. This is illustrated in Fig 5 in which edges are represented by points for 2D geometry and in Fig 6 for a full 3D configuration. The mid surface of cells i and j ($MS_{O_{V_{ij}}}$) can be defined and extracted from the local Voronoi-like level set function associated with the two considered cells i and j (Figs 5(a) and 6(a)). According to the proposed algorithm, an initial *triangulated mid surface* ($MS_{O_{V_{ij}}}$) for cells i and j is extracted by using a marching cube method from the function $O_{V_{ij}}$ [38] defining an explicit surface geometry. The outcome represents a discretization of the surface located between the two cells i and j , but without accounting for the other cells ($k \neq \{i, j\}$), as shown in Fig 5(a) as a bold line. Because of the presence of other cells in the RVE, the obtained initial mid surface between i and j ($MS_{O_{V_{ij}}}$) must be cut by the walls of the other cells ($MS_{O_{V_{ik}}}$). The different neighbouring cell walls are therefore successively used to cut $MS_{O_{V_{ij}}}$, as shown in Fig 5(b-h) by considering the other cells one by one. As illustrated in Fig 5(j-k), by applying the proposed cutting operations on all of the cells (the dashed part of $MS_{O_{V_{ij}}}$ is removed by cuts), a description of the actual cell faces of the RVE is eventually obtained.

The cutting operations of the mid surface $MS_{O_{V_{ij}}}$ by the neighbouring cells mid surfaces $MS_{O_{V_{ik}}}$ is explained in more details in the following. The initial triangulated mid surface $MS_{O_{V_{ij}}}$ is extracted. Then for each neighbouring cell k , $k \in [1 : n]$, $k \neq \{i, j\}$, the value of the ($O_{V_{ik}}$) level set function is evaluated on the vertices of the $MS_{O_{V_{ij}}}$. This evaluation can be interpreted as calculating the distance of the vertices ($Df_{triangle}^{vert}$) of the triangulated surface $MS_{O_{V_{ij}}}$ to the mid surface $MS_{O_{V_{ik}}}$. The $MS_{O_{V_{ij}}}$ vertices with negative distance values are considered as being located inside $MS_{O_{V_{ik}}}$ (where $O_{V_{ik}} < 0$) and are kept, while vertices with positive distance values are being discarded (see Fig 7). It is worth mentioning that the deduced level set function $O_{V_{ij}}$ has a sign contrary to the global level set function O_V obtained from global distance fields DN in equation (1). As shown in Fig 8, this procedure splits the boundary triangles of $MS_{O_{V_{ij}}}$ (triangles with different distance field signs at their vertices) into two parts. New vertices and triangles are created where the sign of the distance field ($Df_{triangle}^{vert}$) changes. The cutting line can cross the original triangle vertices in two different cases: 1) two vertices of the triangle are inside and one vertex is outside of the $MS_{O_{V_{ik}}}$; in this case two new triangles are created and added to the triangulated surface $MS_{O_{V_{ij}}}$; 2) if only one vertex lies inside $MS_{O_{V_{ik}}}$; in this case only one new element is created as a subtriangle of the original one and added to the triangulated surface $MS_{O_{V_{ij}}}$.

This cutting process to obtain the target face in a 3D RVE is illustrated in Fig 6. During this process, edges vertices are saved in a different data structure in each cutting step and get updated continuously. Therefore, on the obtained target face $F_{MS_{ij}}$, each edge ($E_{F_{ij}}^k$)—consisting of different vertices—is associated with the corresponding k value, where k is the cell number that created the edge on this target face. In other words, $E_{F_{ij}}^k$ means that an edge belongs to the face $F_{MS_{ij}}$ between cells i and j and that this edge was created by cutting by a face of cell k .

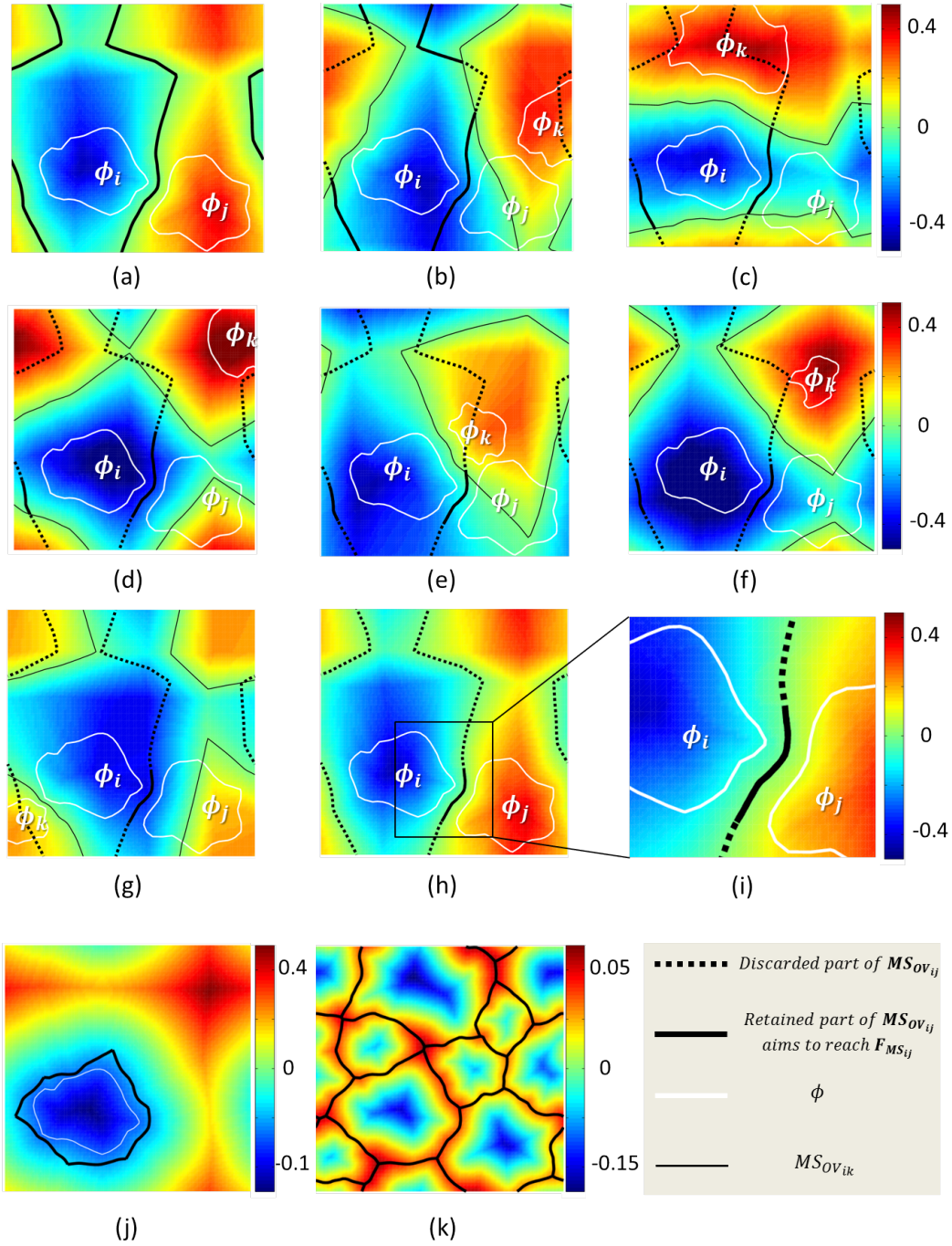


Figure 5: A 2D illustration of the cutting operation. (a-i): producing the face ($F_{MS_{ij}}$) between cells ϕ_i and ϕ_j by cutting the ($MS_{OV_{ij}}$) due to the presence of other cell walls ($MS_{OV_{ik}}$). (j-k): illustration of the generated faces for a cell and for a whole 2D RVE. Faces and edges are represented in 2D by lines and points, respectively.

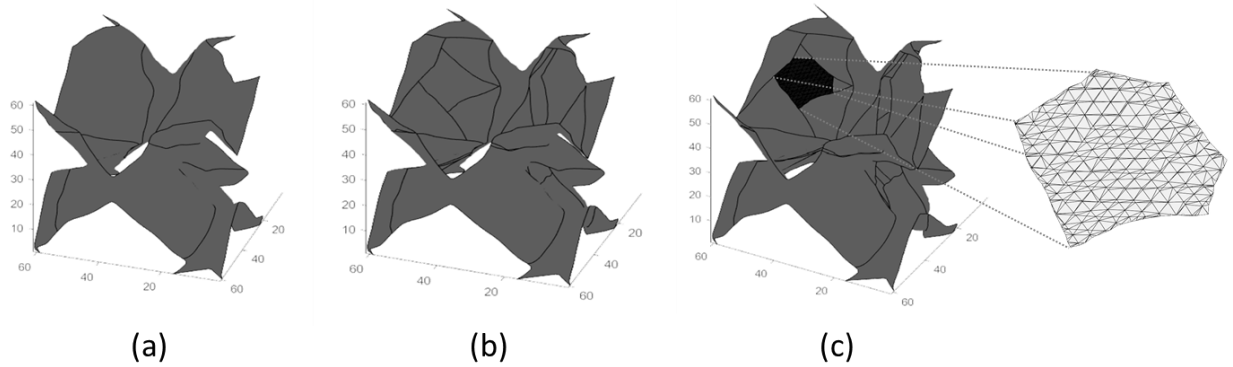


Figure 6: 3D illustration of cutting process of a mid surface ($MS_{O_{vij}}$) due to the presence of other cells to obtain the cell face ($F_{MS_{ij}}$) between cells i and j .

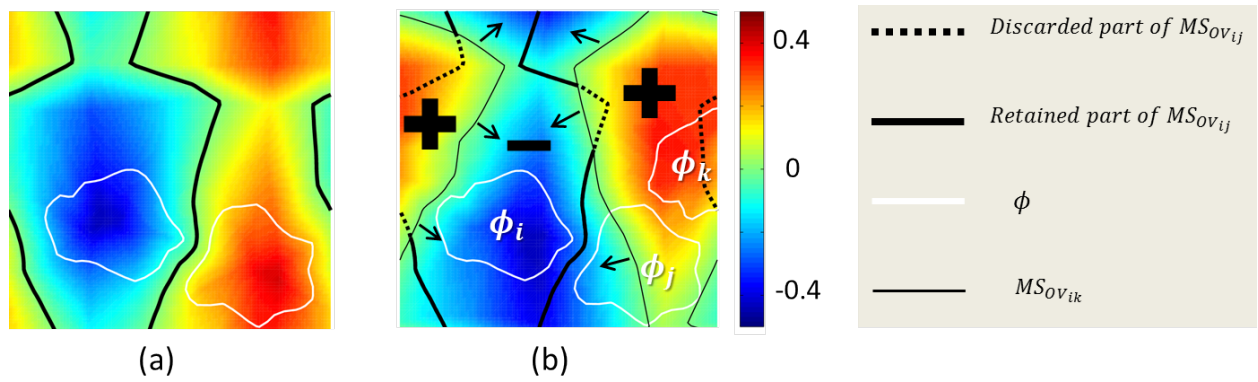


Figure 7: A 2D illustration of the cutting a $MS_{O_{vij}}$ (a) due to the presence of one neighbour cell (b). The parts of the $MS_{O_{vij}}$ that are located inside the $MS_{O_{vik}}$ (shown with arrows) are kept and the rest is discarded. The faces and the edges in 3D are represented here in 2D by lines and points, respectively.

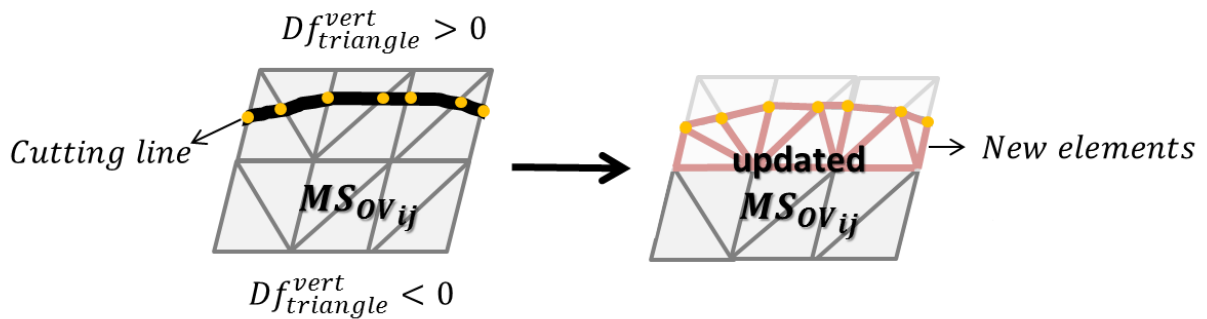


Figure 8: Schematic procedure for building the new elements and vertices (right) at the cut elements (left) during the cutting operation of $MS_{O_{vij}}$.

The corner points, common to two adjacent edges, are also determined and are sorted for each face. A corner point is defined as a point that is shared by two edges on a face. Based on the presented procedure, an explicit discretized description of the faces is created for each cell wall based on the initial triangulated surface obtained from the marching cube extraction. This description is of rather poor quality as shown in 6(c). Due to the grid resolution used for the level set functions evaluations, the extracted faces are disjoint: small gaps appear between the corresponding edges on adjacent faces and the positions and number of vertices along edges common to two faces do not match. An additional procedure is thus required to stitch those discrete faces together and improve the quality of the representation.

2.2.2. Construction of an open foam-like structure using cell edge stitching

Generally, in the generated closed cell foam RVE, an edge is shared by at least two faces, assuming that the external faces of the RVE are also considered as faces. A merging strategy is needed to stitch the extracted discrete faces together by making their common edges description unique. To connect the obtained faces, with their corresponding edges and the corner points, the idea is thus to construct the frames of those faces first, and then to collapse them in a single structure by removing the repeated or very near points.

For each face edge, a new set of equally distanced points are added between corner points along a straight line. In the case of a highly curved edge, it is divided first into two segments and then two new sets of equally distanced points are added to keep the distance relatively the same after the points are moved from this straight line to the actual curved shape of the edge. This chosen interdistance between points on a straight edge is referred to as frame mesh size parameter, L , and is a user input.

These edge points along straight line are then pushed away iteratively toward the actual position of the edge according to their level set information (Fig 9). The displacement direction (outward or inward) of these points in the positioning process (shown by arrows) is dependent on both the convexity and on the magnitude of the edge curvature. This process is iterative because the level set functions used here are no longer signed distance fields (they are combination of signed distance fields). As a result they do not have the property $|\nabla(DS_i(\mathbf{x}))| = 1$ that would allow positioning the points in a single operation to the curved edge. Three level set functions $O_{V_{ij}}$, $O_{V_{ik}}$ and $O_{V_{jk}}$ are used, as illustrated in Fig 10. Each point (grey circle) has to be positioned on the zero level set of these three functions simultaneously. The meshed frame of a single cell face is illustrated in Fig 9. The frames are meshed/built in such a way that frame edges of the different intersecting faces are associated the same number of points with the same coordinates on the curved edge (within the grid resolution of the domain). An open foam-like frame structure results from collapsing the corresponding edges of different faces to a single shared edge as the next step (Fig 11). The resulting frame points (Fig 11) in addition to the points on the faces $F_{MS_{\alpha\beta}}$ (Fig 9) are considered as the point cloud used in the shell meshing process for reconstruction of the cell faces in the subsequent operations, see Section 2.2.4.

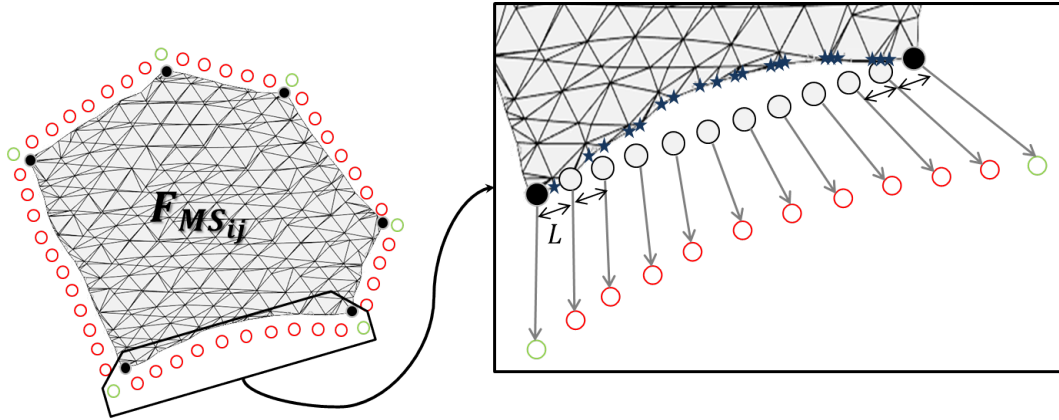


Figure 9: Example of the frame discretization of an extracted cell face ($F_{MS_{ij}}$). The frame points (red circle) and junction points (green circle) are positioned according to (Fig 10). Corner points and edge points for a single edge are shown in filled black circle and blue star shape, respectively. The points displacement vectors are magnified here for the sake of illustration.

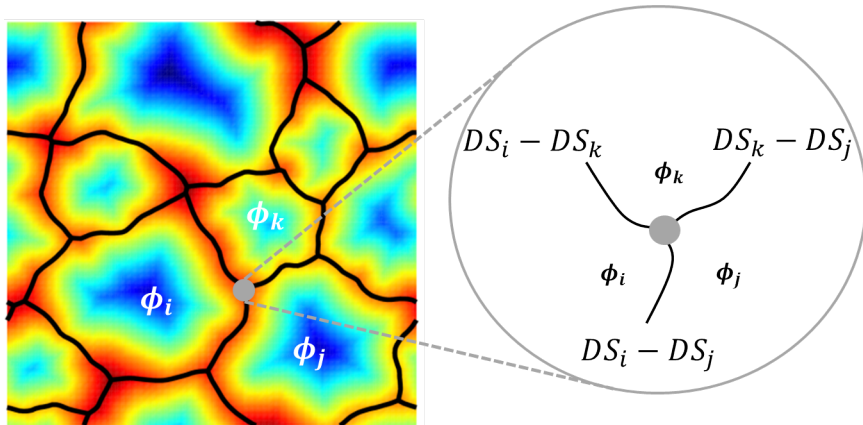


Figure 10: Positioning of the frame points by using the corresponding cell distance fields. Three level set functions of $O_{V_{ij}}$, $O_{V_{ik}}$ and $O_{V_{jk}}$ are used in the pushing process.

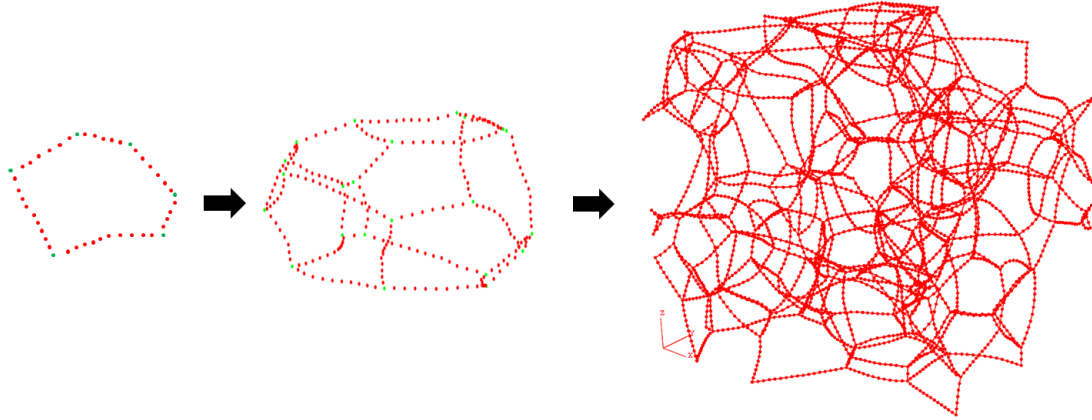


Figure 11: Construction of an open foam like structure by combining/collapsing the faces discretized frames of cell faces.

2.2.3. Point cloud smoothing

The point cloud for each face now consists of the points on the face $F_{MS_{ij}}$ and the frame points generated in Section 2.2.2 (Fig 9). In general, a good quality mesh can not be obtained from this automatic procedure, and often ill-meshed surfaces with badly shaped elements appear. This, at least in part, is the result of the marching cube procedure. Since the point cloud on the faces is most often completely unstructured, it causes many problems such as sliver elements or mesh defects in the face reconstruction process, *i.e.* the finite element meshing of the surface, if the points are directly used as finite element nodes.

Having a more structured point cloud on the faces is therefore crucial to reconstruct the faces for a good mesh quality. To achieve this, based on the frame discretization size (L), two distance tolerances ($Tol1$ and $Tol2$) are defined to find and eliminate the unwanted points from the point cloud. To homogenize the point cloud to obtain proper elements shapes (*i.e.* obtain similar distances between points that will become nodes), the points close to the frame up to a pre-defined threshold criterion ($Tol1$) are eliminated. Likewise, the points on the face with a distance less than $Tol2$ are merged. This simple procedure produces a relatively uniform distribution of the points on the face being a requirement for the surface meshing algorithm used subsequently.

2.2.4. Surface meshing

The surface meshing adopted here is a process analogous to constructing triangular elements from a set of scattered points. Meshing methodologies can generally be divided into two main categories: implicit (*e.g.* Poisson method, see [39]) and explicit methods. Explicit methods triangulate the points directly, and are classified in two main classes, *i.e.* Voronoi/Delauney-based methods and mesh-growing approaches [40, 41]. These methods are faster but less robust

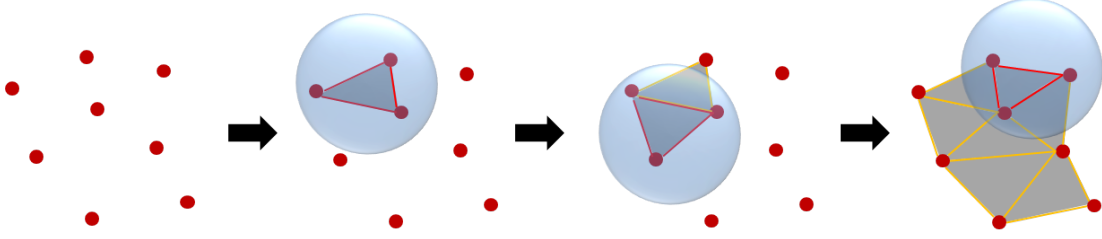


Figure 12: Intuitive illustration of ball pivoting algorithm for surface reconstruction from a point cloud [41].

in comparison with implicit methods. Implicit methods however require more geometrical information than the point cloud coordinates (*e.g.* normals to the surface) to construct the mesh. The major drawback of implicit methods is the high risk of losing the geometrical details.

For the reasons above, the Ball Pivoting Algorithm (BPA) [41] was employed here. It is a mesh growing algorithm, powerful for meshing a surface starting from a uniformly distributed cloud of points. This method, unlike the Voronoi/Delauney-based methods, is more suitable for meshing open surfaces, which is the case of cell faces here. The reliability and the robustness of this approach strongly depend on the homogeneity of the point cloud. In spite of the smoothing of the point cloud *a priori*, an additional post processing procedure therefore was also implemented to check the mesh quality on the faces and, if needed, to repair the possible defects.

The BPA incrementally builds an interpolating triangle between input points of the cloud using the points cloud coordinates and a ball radius R , which is taken as a parameter. The algorithm starts from a seed triangle for which the ball of radius R is touching the three points without containing any other points of the cloud. The other triangles are subsequently built one at a time by performing the pivoting procedure on each triangle edge. The pivoting process is defined as the continuous motion of the ball, during which the ball remains in contact with two points and allows finding the nearest adjacent point. The BPA is shown in Fig 12 schematically. In this process edges can be flagged as being on the boundary (*i.e.* no more pivoting is possible) or as being active.

In a complex closed cell foam RVE it is more convenient to reconstruct/mesh the faces one by one to ensure robustness (*i.e.* avoid self intersecting elements and missing elements). Therefore, at each single face meshing step, the input point cloud is defined as the set consisting of the homogenized network of points on the face together with the discretized frame points around that face. The resulting point cloud is meshed using the BPA available in Meshlab [42]. The process starts with a chosen initial guess for the ball radius $R = L$. The constructed surface is then examined, checking for self intersected elements by using the Tetgen subroutine [43]. In case of self intersecting finite elements the whole meshing step for the face is restarted with an increased ball radius $R + \Delta R$, in which $\Delta R = 0.3 R$, until a mesh without self intersection is obtained. The connectivity of the model is checked next, searching for missing/redundant

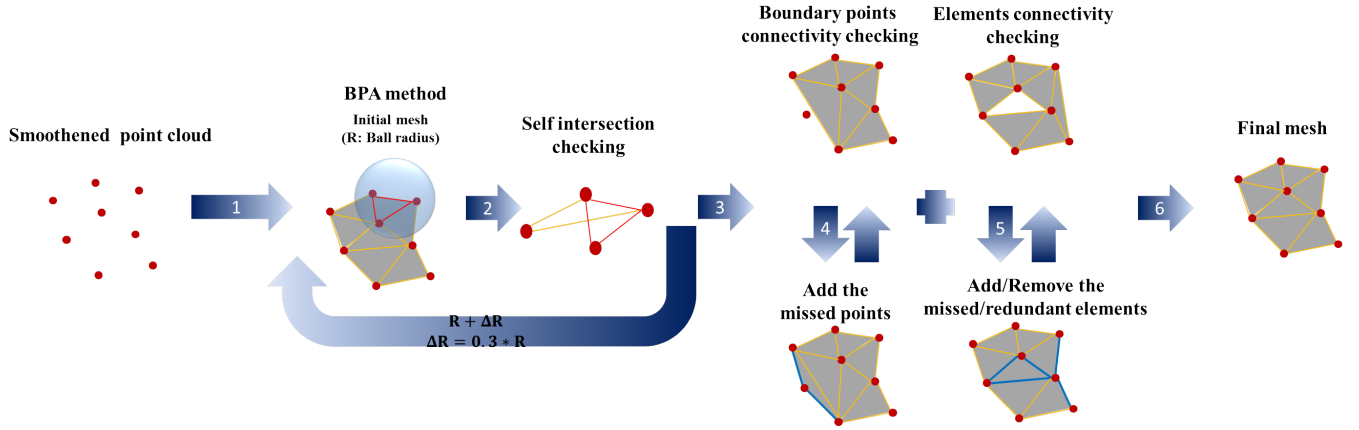


Figure 13: General meshing strategy used to reconstruct the faces from the smoothed point cloud at each single face meshing step.

elements or missed boundary points. Defects in connectivity are repaired in a post-processing step as explained in Section 2.2.5. Finally, the newly meshed face is added to the finite element mesh of the RVE by updating the mesh data structure (nodes coordinates and connectivity matrix). The complete meshing algorithm is presented in Fig 13.

2.2.5. Post processing of the RVE mesh

In general, surface meshing methods do not guarantee a perfect tight triangulation. In particular the BPA method has shortcomings in accuracy when the point cloud is not distributed close to uniformly on a face and the face geometry is complex. It is crucial that the meshed face keeps the same number of frame points as the input, to guarantee conformity at the edges common to several cell faces (walls). A final mesh post-processing is thus implemented to detect any missed boundary point, missed element, or redundant element; and to repair them.

In order to find the defects, the obtained mesh (for each face) is checked for edges appearing only once in the connectivity matrix. In a defectless mesh, the result would be the list of the face boundary edges only. The connectivity of the frame and the number of its points are data known *a priori* from section 2.2.2 in the input point cloud. The finite element mesh edges and edge points are compared to the known frame edges and points and if they do not correspond perfectly, the extra finite element edges are tagged as defect and are referred to as front edges. Besides, the possible missed frame points are also flagged.

The front edge points and the missed frame points are considered as orphan points. In each mesh repair iteration, starting from a front edge, missed finite elements are constructed from a front edge and the nearest neighbour orphan point, as shown in Fig 14. The resulting new finite element is added to the mesh, see Fig 14 (a), (b) and (d). In case of excess finite elements (*i.e.* bridging spuriously edges, as in 14(c)), the finite element at the front edge and the nearest orphan point already exist in the mesh. Such elements are eliminated from the mesh (Fig 14(c)). This process

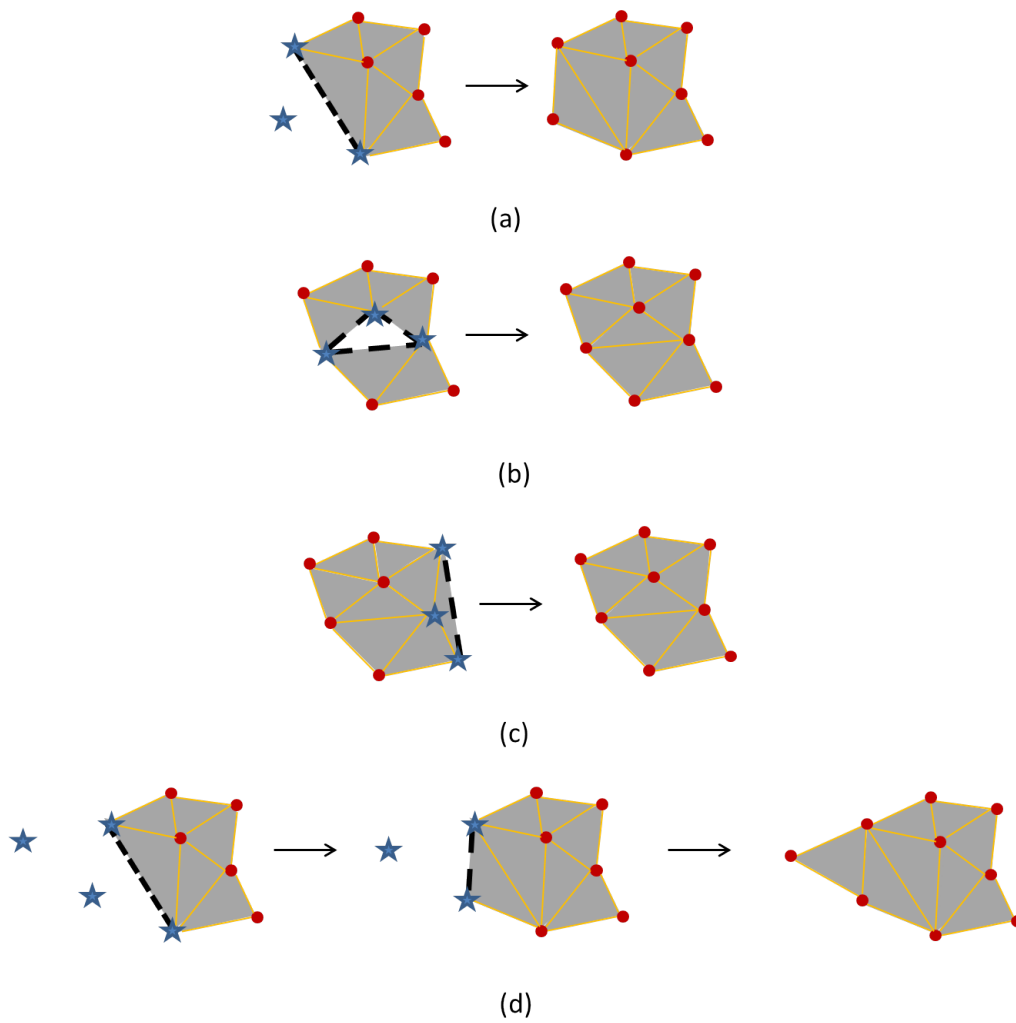


Figure 14: The possible meshing defects and corresponding repaired mesh after mesh post processing: (a) a missed frame point, (b) a missed element, (c) a redundant element and (d) missed frame point and a missed element. The dashed line is considered as front edge and the star shaped points are orphan points.

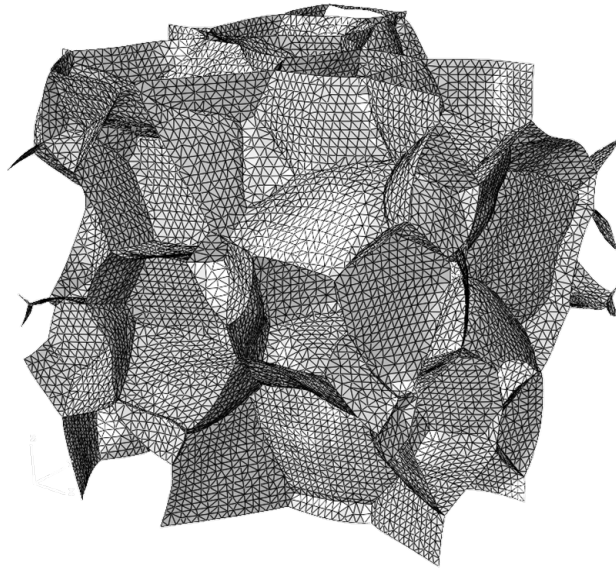


Figure 15: Example of surface geometry with triangular shell elements for the RVE with 26 cells, 357 cell walls, 21511 nodes and 43472 elements.

continues until no additional front edge is detected. A meshed surface geometry with triangular shell finite elements obtained with this procedure for a closed cell metallic foam RVE is illustrated in Fig 15.

The computing times for the RVE generation, 3D meshing, shell geometry construction and its meshing are in the order of tens of minutes. The generation and the meshing processes are executed on i7 CPU and coded in an interpreted language (MatLab), which should of course be accounted for when interpreting the computing times. Indeed, recoding the routines in a compiled language would improve the computation time dramatically with respect to the current computation time.

3. Finite element modeling

The main steps of the global procedure to produce both the 3D and shell closed cell metallic foam finite element models are illustrated in Fig 16. The characterization of relevant morphological indicators of closed cell metallic foams was given in a previous effort [31], showing that different randomly generated microstructures yield similar results when the same set of morphological indicators is used. The foam RVEs and the set of morphological indicators used in the present contribution are based on a significant body of literature presenting experimental evidence about ALPORAS foams, see for instance [8, 37, 10].

The shell models are extracted from the 3D periodic implicit RVE geometry. Maintaining the same morphology, volume and location of the cells was chosen to allow comparing the shell model performance directly with previous

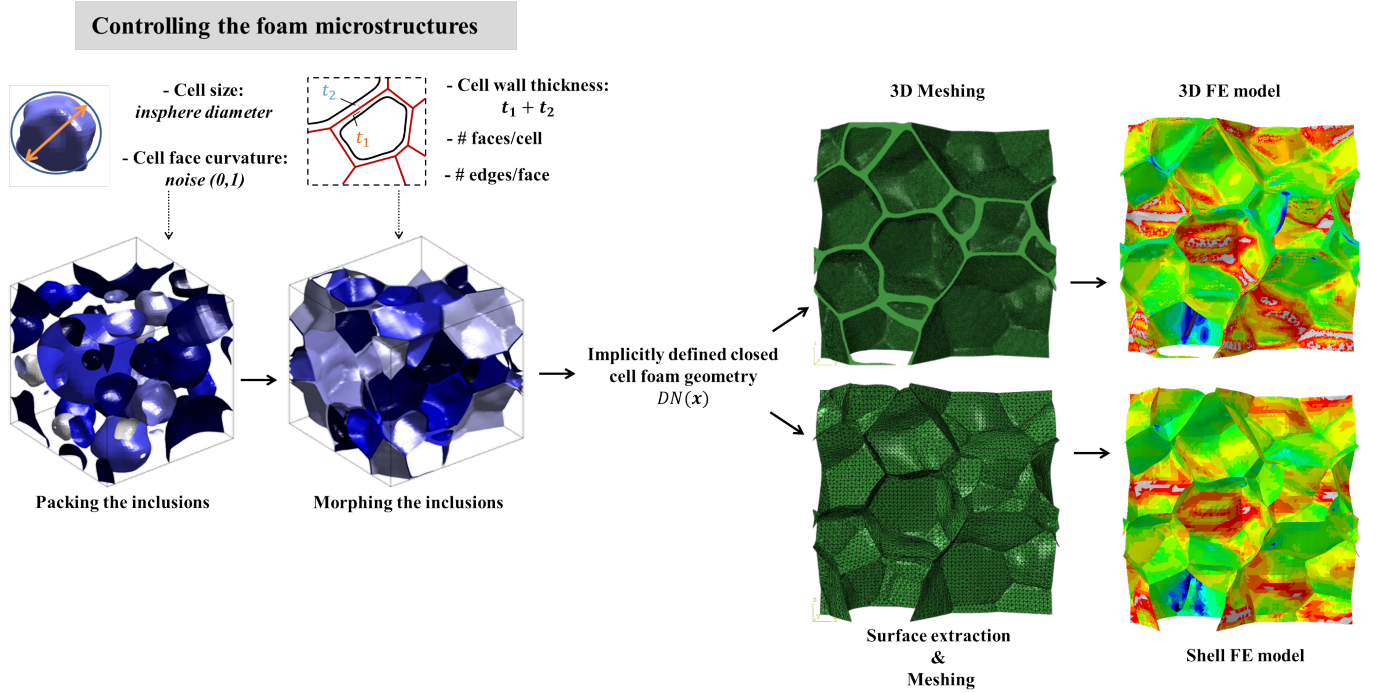


Figure 16: Required steps to obtain closed cell foam 3D and shell finite element models starting from a packing of the inclusions and their morphing with a morphology controlling procedure.

results obtained with a 3D model. The nodal shell thickness values are directly extracted from the 3D implicit geometry so as to maintain a correct volume fraction of the material. At each node—including the nodes shared by two cells on an edge and shared by three cells at junction lines—the distances to the first and second neighbour cells ϕ_i and ϕ_j , are computed based on the global distance fields information, *i.e.*, $DN_1(x)$ and $DN_2(x)$. Therefore, two nodal shell thickness values with respect to the surface geometry are obtained, denoted as t_{DN_1} and t_{DN_2} . These values are summed for each shell node to obtain the total nodal shell thickness. In this way, the cell wall thickness variation along each cell wall is incorporated in the shell description.

However, due to material overlapping at the junction lines (intrinsic to shell modelling) as shown in Fig 17, it is not possible to achieve the same volume fraction as the reference 3D model. The shell volume fraction can be corrected phenomenologically, as will be discussed in Section 4. The discretization of the shell surface is made with S3R finite elements of ABAQUS [44]. This is a 3-node triangular general-purpose shell finite element that accounts for finite strains with six degrees of freedom per node (translations and rotations). This element can be used for both static incremental analysis and explicit dynamics. The former option is used in the analyses presented in Section 4. The latter one is chosen in the analyses described in Section 5 to allow the incorporation of cell wall contact. All the tests were performed in ABAQUS [44] on a high-performance cluster with three computing nodes (each with a 24

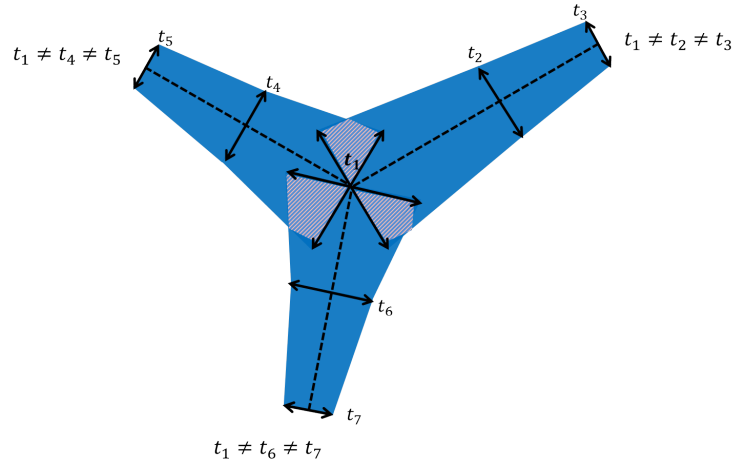


Figure 17: Schematic representation of the overlapping material at cell junctions when using shell finite elements with different nodal thicknesses (cut view).

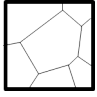

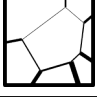

Intel(R) Xeon(R) E5-2620 v2 2.10-2.60 GHz processors) and with 64 GB RAM.

Microstructural deformation modes of ALPORAS were reported in [45]. They include bending and formation of plastic hinge in the cell walls, cell wall plastic tensile stretching and buckling as well as cell wall fracture. It should be noted that in spite of the possible appearance of high generalized stresses (bending moments) at junctions, the experimental deformation and failure mechanisms are observed to occur mostly in the cell walls due to their much lower thickness with respect to the strong and thick junctions. According to [45], cell wall fracture is thus a possible failure mode in the experiments, however it is disregarded in the present numerical simulations because (i) the current numerical ingredients (elasto-plastic behaviour, finite strain and contact) capture the global and local behaviour of the closed cell foam properly as will be shown and (ii) treating fracture computationally is very complex, potentially requiring XFEM type of approaches or higher order theories with strong mesh refinements. Two types of simulations are therefore considered in this work:

1. A computational assessment of the effect of the morphological features on the overall mechanical response of the material is performed under quasi static compressive loading up to 5% macro strain (Section 4). In such simulations, it was verified that no contact is activated, but local buckling and plasticity occur in walls. The results of shell-based simulations are compared to full 3D finite element models, focusing on the computational accuracy and efficiency.

Computational homogenization is employed in these simulations to compute the effective averaged material response of the RVEs [46] by applying periodic boundary conditions on the external boundary nodes of the RVE through linear dependency equations (both displacement and rotation DOFs are coupled periodically for

Table 1: Simulated cases incorporating the effect of different morphological fine scale features; ϕ represents the cell size distribution, t_{wall} the wall thickness distribution and $\theta_{\text{cell wall}}$ the average wall curvature.

Tests	ϕ dist.	t_{wall} dist.	$\theta_{\text{cell wall}}$	ϕ & t_{wall} link
S 	✓	—	—	—
SC 	✓	—	✓	—
STL 	✓	✓	—	✓
STLC 	✓	✓	✓	✓

shell RVEs). These boundary conditions are frequently used in the literature and the interested reader is referred to the following works and references therein for more details [47, 48].

The varied parameters for these simulations are summarized in Table 1 and the corresponding RVEs are shown in Fig 18. The capital letters denoting each simulation describe the corresponding incorporated features as follows:

- In simulation **S**, the proper experimentally reported cell size distribution [37] is used with a constant cell wall thickness and without introducing cell wall curvature. This RVE is taken as the reference for comparing the morphological features effects presents in the following.
- In simulation **STL**, a random allocation of wall thicknesses is used, in which the cell wall thicknesses are constrained match the cell sizes as these two distributions are correlated [49].
- Simulation **SC** is performed incorporating only the cell size distribution, but with an increase of the cell wall curvature (noise=0.1).
- Simulation **STLC** incorporates simultaneously all the geometrical features mentioned above.

2. The evaluation of the mechanical response of a closed cell foam up to 65% macro compressive strain is next performed using the shell model (Section 5). All three strain ranges including densification are covered here, incorporating contact geometrical nonlinearities and elasto-plastic material behaviour in the computational model,

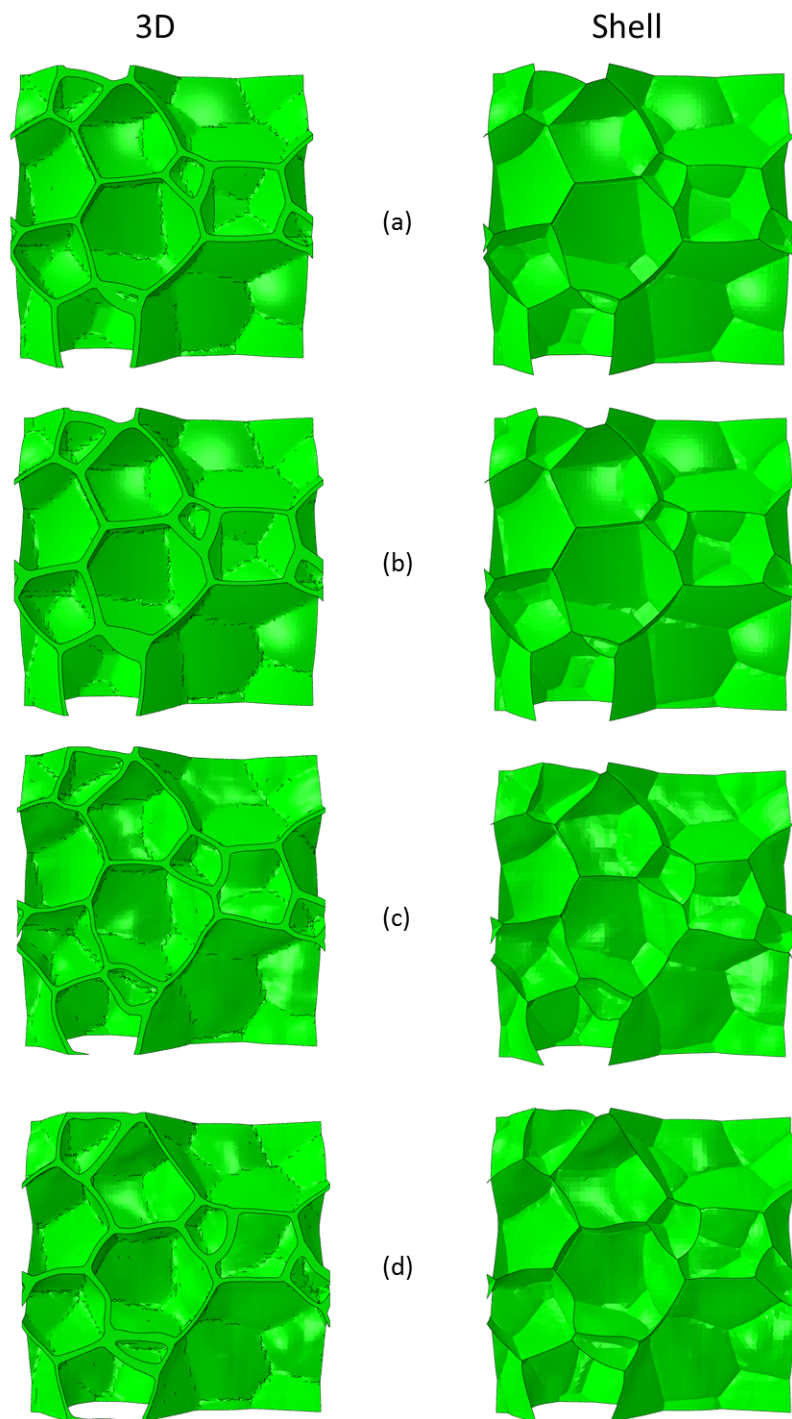


Figure 18: RVEs of size $15\text{ mm} \times 15\text{ mm} \times 15\text{ mm}$ with 3D finite elements (left) and shell finite elements (right) for the different morphologies given in Table 1. a) S; b) STL; c) SC; d) STLC simulations.

Table 2: Mechanical properties of cell wall material for ALPORAS closed cell foams [50].

Poisson's ratio	0.3
Young's modulus (GPa)	68
Yield stress (MPa)	35.5
plastic hardening exponent (m)	8.5

using the explicit solver of ABAQUS. In this simulation no periodicity is applied to mimic the experimental boundary conditions from [8]. The models were sandwiched between two parallel rigid plates, with the other four (lateral) faces of the specimen left free in the simulation. During the compression process, the top rigid plate is moved downward with an constant velocity while the bottom rigid plate is kept fixed. The rigid body modes of the model were, of course, also constrained to ensure the well-posedness of the problem.

Due to the static setting (Section 4) and the slow loading conditions in the explicit simulation of the compression test (Section 5), the cell wall material is assumed here to follow a strain rate-independent isotropic hardening plasticity model [50, 51] as

$$\bar{\epsilon}^p = \frac{\bar{\sigma}_Y}{E} \left(\frac{\bar{\sigma}}{\bar{\sigma}_Y} \right)^m \text{ for } \bar{\sigma} > \bar{\sigma}_Y \quad (3)$$

where $\bar{\sigma}_Y$ is the yield stress, $\bar{\epsilon}^p$ is the equivalent plastic strain and m is the power law hardening exponent given in Table 2. Note that the rate dependency of material behaviour may become important when such materials are subjected to high strain rates, as in impact loading *e.g.* in shock absorbers [52]. Considering the quasi-static loading conditions here, strain rate dependency was not incorporated in the constitutive model.

In Section 4, all of the simulations were conducted with displacement control of the RVE control points, therefore prescribing the macroscopic strain.

4. Effect of morphological features on the mechanical response

The effects of the morphological indicators on the macroscopic response of the foam material are investigated now by using the shell-based model to assess the implications of the assumed shell kinematics on the ability of the model to capture their influence. While the kinematically richer 3D model, exactly incorporating cell junctions geometry, was shown earlier to be sensitive to each morphological effect separately [31], this still has to be established for the shell-based approach. The goal of this section is, thus, to investigate the accuracy of the shell formulation in the prediction of both the macroscopic response and the micro scale deformation and failure mechanisms. This is achieved by comparing it to the full 3D model, taken as reference.

The shell formulation is established on the following classical geometrical and kinematic assumptions: (i) the ratio of thickness to the spans must be less than $\frac{1}{10}$ (referred to as assumption H1 in the sequel), (ii) the plane sections remain

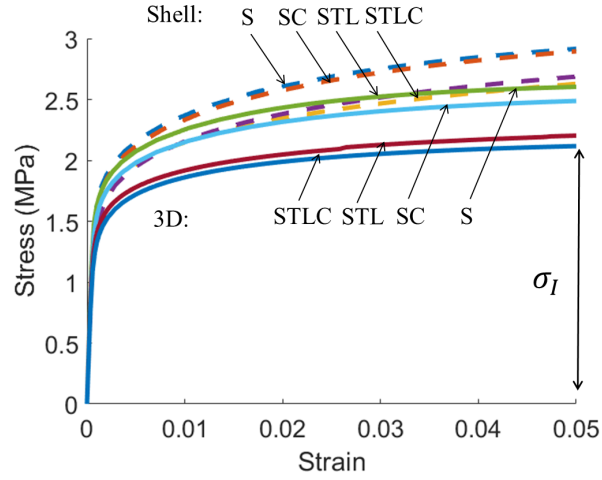


Figure 19: Macro scale stress-strain response of RVEs obtained with computational homogenization for different morphological effects (Table 1). dashed lines: shell and full lines: 3D. The 3D model volume fraction is 10.4 % and the obtained shell model volume fraction is 11.2%.

plane after deformation (referred to as assumption H2 in the sequel), in other words, the director vector direction along the shell thickness remains straight (but not necessarily normal) in the deformed configuration (Reissner-Mindlin assumption). As a result, the in-plane strain variation through the thickness is, at most, linear; and (iii) the stress in the director vector direction is zero.

The macro scale averaged stress-strain curves obtained by computational homogenization with periodic boundary conditions for the shell and 3D geometries are shown in Fig 19 for simulations incorporating different morphological effects. It is observed that all the incorporated microstructural geometrical features, *i.e.*, cell size distributions, wall thickness and curvatures, have their specific influence on the response (the same influence appears in both the 3D and the shell-based models). For each morphological variation of Table 1, the Young's modulus and the σ_I plateau stress level for both the shell and the 3D models are listed in Table 3. The macro yield stress plateau is different for the shell and the 3D models, as illustrated in Fig 19. This difference will be shown to be reduced when a volume fraction correction is performed in the shell models. Due to the later development of plastic deformation in the shell model, the gap between the shell based and the 3D simulations increases as the global strain increases.

Among the considered parameters in the shell models, the cell wall thicknesses linked to the cell sizes in the cell distribution of the RVE has the most significant effect on the σ_I stress level. This is in agreement with the findings from the 3D model, as reported in [31]. According to the obtained results, in general, the shell models slightly underestimate the RVE Young's modulus (up to 6.6%) and overestimate the σ_I macroscopic plateau stress level at 5% strain (up to 24%) in comparison with the reference 3D models.

Table 3: Comparison of the resulting macroscopic material properties obtained from 3D and shell models for $V_F^{3D} = 10.4\%$ and $V_F^{shell} = 11.2\%$.

	Young's Modulus (GPa)			σ_I (MPa)		
	3D	Shell	Modelling Error (%)	3D	Shell	Modelling Error (%)
S	2.57	2.4	-6.6	2.6	2.91	11
SC	2.4	2.29	-4.5	2.48	2.89	16
STL	2.3	2.21	-3.9	2.2	2.68	21
STLC	2.1	2.09	-0.4	2.11	2.62	24

The differences between 3D and shell models results originate from different sources. Unlike the 3D models, in the shell models, the cell junctions are only crudely described. The shell faces are connected only along a single line which cause a junction stiffness deficiency compared to the 3D model. As shown in Fig 17, the material belonging to different faces connected at a line junction is overlapping in the shell model. Therefore, the extracted surface geometry results in a larger material volume fraction, which is known to be a dominant parameter on the macroscopic material behaviour. As reported in Table 3, the modelling errors differ for the different incorporated morphologies. Therefore, the modeling error with respect to the 3D description is also linked to the shell theory assumptions that are observed to influence the match between the shell and 3D models depending on the 3D model complexity.

To discuss the shell hypothesis H2 (plane section remain plane after deformation) versus the geometry of the cell walls (*i.e.* flat or curved), the ratio of the mean curvature radius/thickness of cell faces is defined as quantity of importance. This ratio is important because the strain distribution through the thickness departs from a linear variation (shell theory) as this ratio decreases. In the simulation **SC**, the initial shape of the cell faces is curved, while in the simulation **STL**, the cell faces are thicker in the smaller cell sizes (most of the cells in the RVEs are medium and small size cells). As a result, the ratio of mean curvature radius/thickness is decreased in simulations **SC**, **STL** and **STLC** compared to **S**. The shell elements in the nonlinear analysis perform thus more accurately with respect to a 3D model in simulations **S** with relatively straight faces than in simulations **SC** with curved cell faces and **STL** with thicker cell faces for smaller cells. Therefore, increasing the complexity of the incorporated features increases the modeling error for σ_I due to the resistance to the free warping (in-plane strain variation more complex than linear). Conversely, this kinematic assumption decreases the modelling error for the Young modulus, because it partially compensates for the junctions stiffness deficiency in the shell models.

The shell model volume fraction (11.2%) can be prescribed to match that of the 3D model (10.4%) phenomenologically, by reducing the thickness uniformly in all of the cell walls by the ratio $\frac{10.4}{11.2}$ (the material overlap at the cell junctions, naturally present in the shell models, of course remains). As reported in Table 4, the homogenized Young modulus decreases further with respect to Young modulus reported in Table 3, but the σ_I values of the shell model get closer to those of the 3D model. Fig 20 shows no considerable difference in the macro yield stress plateau. However,

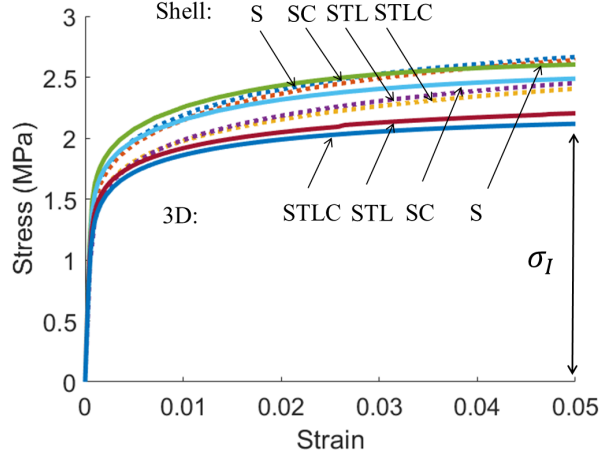


Figure 20: The macro scale stress-strain response of RVEs obtained with computational homogenization for different morphological effects (Table 1). dashed lines: shell and full lines: 3D. The 3D model volume fraction and obtained shell model volume fraction are both set to 10.4%.

Table 4: Comparison of the resulting macroscopic material parameters from 3D and shell FEM for $V_F^{3D} = V_F^{shell} = 10.4\%$.

	Young's Modulus (GPa)			σ_I (MPa)		
	3D	Shell	Modelling Error (%)	3D	Shell	Modelling Error (%)
S	2.57	2.21	-14	2.6	2.66	2
SC	2.4	2.1	-12.5	2.48	2.64	8
STL	2.3	2.04	-11.3	2.2	2.45	11
STLC	2.1	1.95	-7	2.11	2.4	14

the gap increases as the strain increases between the shell based and 3D simulations, because the plastic deformation in the shell model grows slower. Except for simulation **S**, for which the plateau stress prediction for both 3D and shell models is almost identical, the deviations in other cases increases, as the complexity of the geometry increases. The modelling error for the Young modulus is increased after the volume fraction correction. This can be explained by the fact that the cell face thicknesses are decreased while the cell curvatures do not change. This causes lower elastic stiffness in the cells from one hand, as well as an increase in the mean curvature radius/thickness ratio. By comparing the results of the 3D and shell models, the cell wall edges/junctions have been observed to have a strong influence on the obtained macro scale elastic stiffness.

The sources of errors identified as characteristic to the shell description with respect to the 3D modelling can be categorized as follows:

(i) $E_{R_{VF}}$: the overlapping material at the junction lines in the shell description results in higher volume fractions for the shell-based model when using cell wall thickness consistent with the 3D model. In the corrected volume fraction models, the cell wall thicknesses are not identical to the 3D models anymore.

Table 5: Comparison of the computational cost of shell modelling over 3D modelling in a compression test up to 5% macroscopic strain for an RVE with the same base geometry.

Tests	# DOFs	Computation time
STLC-3D	$1250000 \times 3 = 3,750,000$	4 days
STLC-shell	$21511 \times 6 = 129,066$	20 min

(ii) Er_{PB} : in the shell-based models, the faces are connected with each other only at single junction lines, unlike in the 3D models and in experimental observations, where faces are connected through bulky junctions, giving a stronger connection, and consequently resulting in a higher Young's modulus.

(iii) Er_{H1} : the geometry hypothesis H1 of the shell formulation (thickness/span $< \frac{1}{10}$) is not satisfied at all the cell wall edges. Potentially these cell junctions could be represented using beam finite elements for improving the shell model stiffness.

(iv) Er_{H2} : The second hypothesis H2 of the shell formulation, prevents the faces from warping freely in the wall sections. This restricts the possible strain modes in the elements, which can delay buckling and the plastic deformation of the cell walls.

The assessment of the shell-based models was investigated so far in terms of accuracy. It is observed that the shell-based models compared to the 3D models are capable to predict the closed cell foams mechanical behaviour in compression with a reasonable degree of accuracy. The computation time of 3D and shell-based models are compared in Table 5 for the STLC simulation. A speed-up close to a factor of 300 is observed for the shell-based model.

One of the advantages of computational modelling resides in the ability to link the macroscopic behaviour of closed cell foams directly to the micro scale observed cell/wall level behaviour. The deformation and failure mechanisms at the cell level are investigated here by comparing equivalent shell-based and 3D models. Both models are made comparable by using identical cell morphologies (*i.e* the same volume, same position and same wall thickness and curvature). This comparison is used to confirm that the same micro scale deformation patterns are observed, leading to matching macro scale behaviour of both models.

It is observed that, similar to the 3D model, cell collapse initiates on the large cell faces with the smallest thickness. Then, a plastic band percolates in which a set of weak cells are clustered in both models. As illustrated in Fig 21 and Fig 22, the shell-based model captures rather well the plastic regions in the cell faces. The macroscopic plastic band pattern develops similarly in both models, even though the von Mises stress level is lower in the shell-based model than in the 3D model. Plastic deformation in the cell walls occurs mostly because of their buckling. The faces in the shell-based model resist more to the buckling phenomenon because of their higher stiffness linked to the restrictions in the shell kinematics and therefore plastic deformation is also delayed. It is worth noting that the yield lines form far from cell junctions in both models, even though junctions themselves are not accurately represented in the shell-based

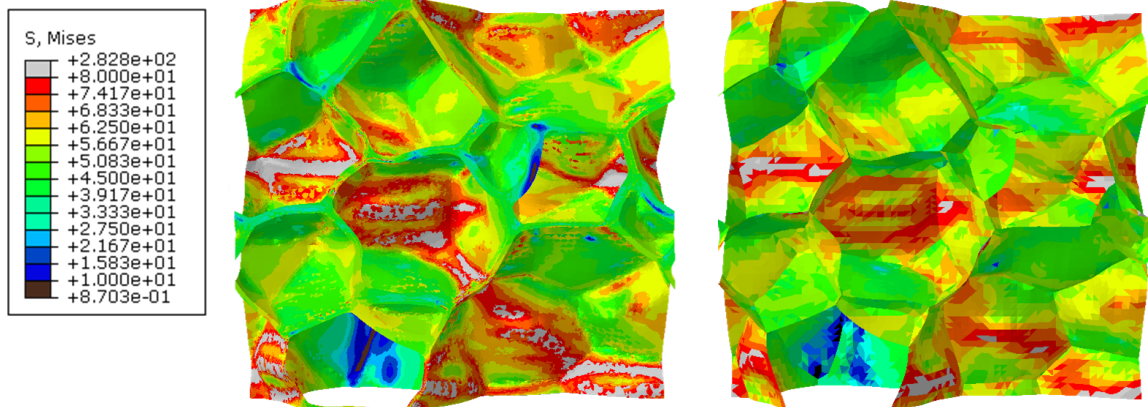


Figure 21: Distribution of von Mises stress at 5% macroscopic strain of 3D (left) and shell-based model (right) (maximum of the stress scale is set to 80 MPa).

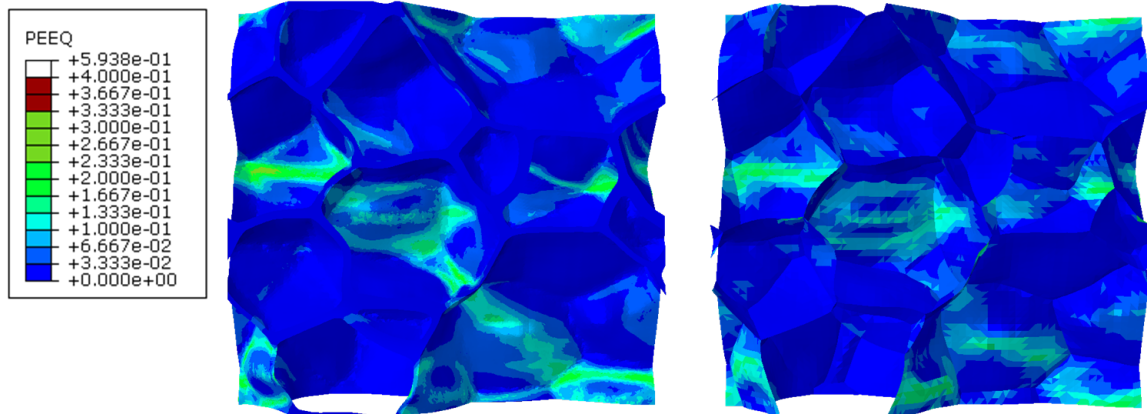


Figure 22: Distribution of equivalent plastic strain at 5% macroscopic strain of 3D (left) and shell model (right) (maximum of the plastic strain scale is set to 0.4).

models. Thus, while junctions are influencing the elastic stiffness, their impact on the plastic deformation is much lower. A slice of the foam in the deformed state is presented in Fig 23 for both models at the same load increment. A good agreement between both numerical responses can be observed. In particular, the shell formulation captures the buckling and bending of the cell walls appropriately.

5. Simulation of a compression up to densification using a shell-based model

The shell-based model was shown in the previous section to be a good simulation strategy with a sound accuracy relative to its very low computational cost for closed cell foams. The high computational efficiency of the shell-based model allows performing more advanced computations compared to a full 3D model. A compression simulation up to

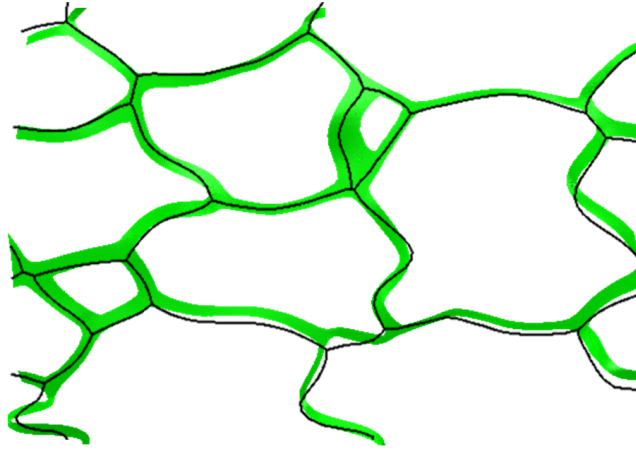


Figure 23: Deformed cross sectional slice of 3D (green) and shell models (black) at the same load increment.

65% macroscopic strain incorporating contact conditions is considered here. Such a simulation would not be feasible using a 3D model due to its prohibitive computational cost.

In order to compare experimental and numerical results on a sound basis, the shell-based model (STLC model) used here was created based on morphological data from the literature for ALPORAS. It is emphasized that the reproducibility of structural results for the same set of morphological indicators was demonstrated previously [31], showing that the specific microstructural realization (specific RVE geometry) considered for the simulations yields results similar to all realizations respecting the same set of morphological indicators. On the other hand, a strain rate-independent isotropic hardening plasticity model is employed for the cell wall material behaviour, which was proposed and exploited successfully for ALPORAS closed cell metallic foams in [50, 51]. Ensuring a proper foam geometry for ALPORAS and a proper constitutive model for the cell wall behaviour is the basis for a direct coupling of the performed simulations to raw experimental data (Force displacement curves in the present case).

The ABAQUS/Explicit software has been used to perform a quasi-static compression test due to its robustness in dealing with contact problems. The general contact feature in ABAQUS is used with a friction coefficient of 0.2 ([53]). A mass scaling method is also used to reduce the computation time by a factor 1000, by means of increasing the density of the base material. To avoid spurious dynamic oscillations, the ratio of kinetic energy to internal energy was kept below 5% in the simulation by using a loading rate of 0.3 mm/s for the imposed macroscopic strain (Fig 24). For the sake of efficiency, the computation time can still be further reduced significantly. For instance by choosing an appropriate macroscopic strain rates (*e.g.* 1.2 mm/s), the complete compression test can be simulated with a reasonable accuracy with respect to experimental results (Fig 25) at an affordable cost (Table 6). For higher loading rates (*e.g.* 3 mm/s), too intense oscillations appear at the beginning of the response curve. The full com-

Table 6: Computation cost for different loading rates imposed on the same shell-based RVE in explicit dynamics simulation.

loading rate	1.2 mm/s	0.3 mm/s
Computation time	8 hours	24 hours

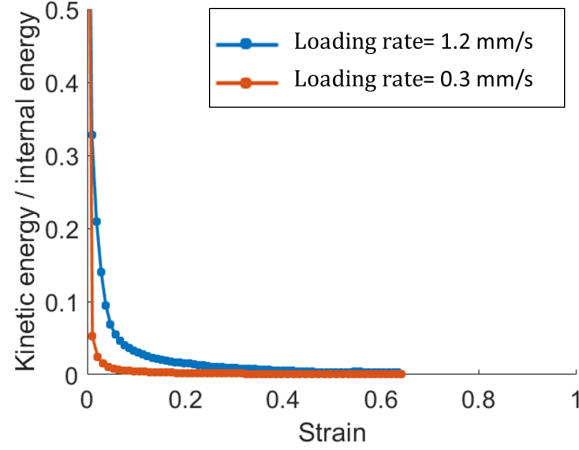


Figure 24: Dynamic explicit simulation of the foam compressive response: ratio of the kinetic energy to internal energy for different loading rates.

pression test has been simulated by solving the equations of motion using ABAQUS/Explicit. Therefore, the inertia effect is a role playing parameter for different loading rates. This led to a response in which the inertia effects increase as the loading rate increases as shown in Figs 24 and 25. By increasing the kinetic energy in each step (Fig 24), an intense oscillatory response is obtained (Fig 25). The ratio of kinetic energy/internal energy was used for evaluating this dynamic effect in the computations. As shown in Fig 24, this ratio is kept to less than 5% at most of the increments in order to exclude artificial dynamic effects in the simulations.

A mesh convergence study was performed in order to ensure the mesh independency of the obtained results. The present results (mesh with 21511 nodes) were compared against the ones provided by discretizations with 12231 and 26088 nodes and it was concluded that convergence was reached, as the differences with the most refined mesh were negligible.

As illustrated in Fig 25, a good qualitative agreement between the experiment reported by [8] and the shell-based simulation is observed covering all three strain ranges of the mechanical response (*i.e.* elastic response, plateau and densification) by considering cell faces contact. The plateau stress level ($\sigma_{pl} = 2.3$ MPa) and densification initiation

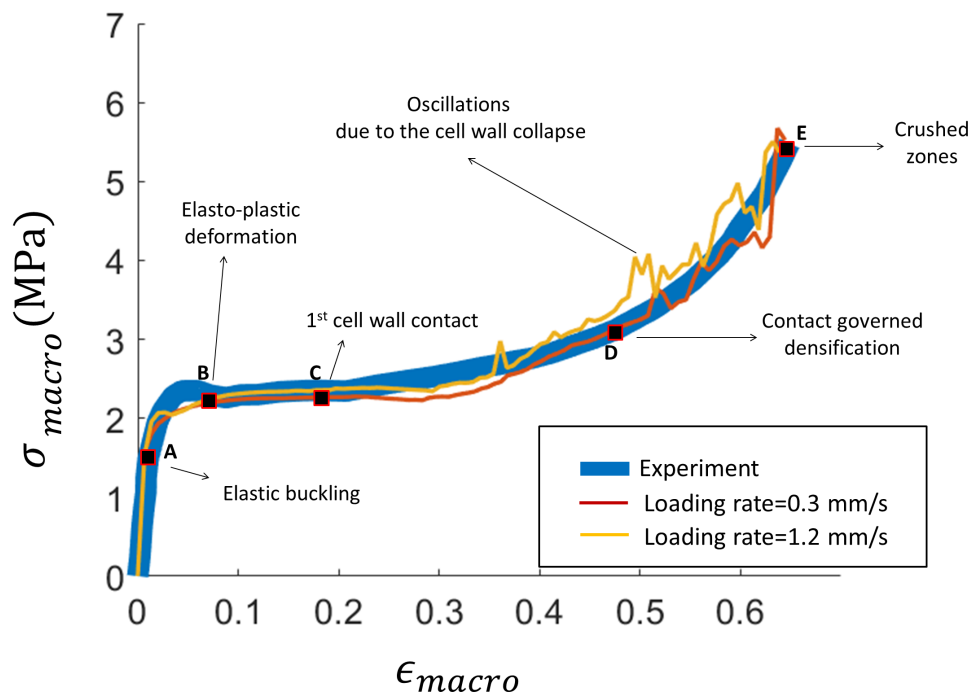


Figure 25: Compressive stress-strain curve from the experiment [8] and the shell-based model for $V_F^{exp} = V_F^{shell} = 12.3\%$ with different loading rates.

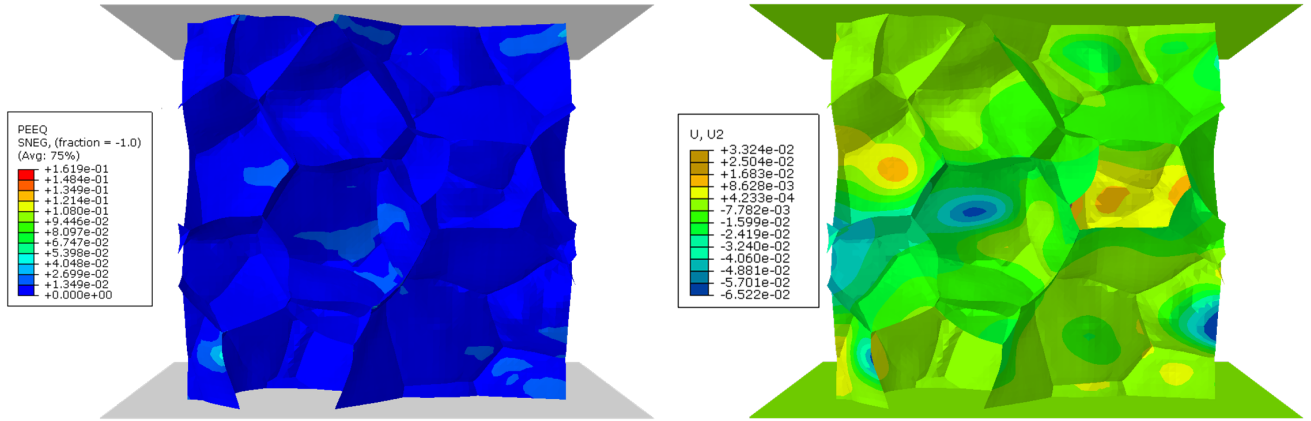


Figure 26: Distribution of equivalent plastic strain (left) and displacement along the y axis (right) at point A of their macroscopic response reported in Fig 25.

(point D) are well predicted by the shell-based model.

The shell-based model is further investigated now to unravel the deformation and failure mechanisms at cell/wall level in different regions and to link the macroscopic behaviour of the closed cell foam to these local deformation mechanisms in the three regimes of deformation. Each regime is associated with specific deformation mechanisms at the local scale. Five points, denoted from A to E, are chosen for this purpose at different macroscopic strain levels on the response curve (Fig 25).

At the transition point A ($\epsilon_{macro} = 0.06\%$) between elasticity and the plastic band formation, most of the cell faces are deformed elastically with only a few faces exhibiting plastic strains, as shown in Fig 26. As compression proceeds further, plastic deformation spreads especially in the buckled cell faces. The macroscopic stress level remains almost constant at this stage. Three points (B, C and D) specified on the plateau stress level correspond to three successive macroscopic strain levels, for which the local equivalent plastic strain distributions are given in Fig 27 (B-D). The plateau region, see Fig 25 (B-D), is the most important one in the foam response for energy dissipation. The plastic zones of several faces are connected and form a weak zone that crosses the RVE, as shown in Fig 27 (B-C). However, the cells outside this plastic band, almost keep their initial shape at this stage.

After the deformation of a cell face, the load is transmitted to another cell face. This process absorbs energy without considerable change in the macroscopic stress level. The amount of absorbed energy is directly associated to the cell failures and collapses. Thus the size of the cells and cell faces located in the weak zone is influencing the energy absorption capacity.

At point C, in addition to the plastic deformation and buckling of the faces, contact between faces is also established. The contact area is increasing while the plastic band spreads in the weak zone. From point D to point E, a

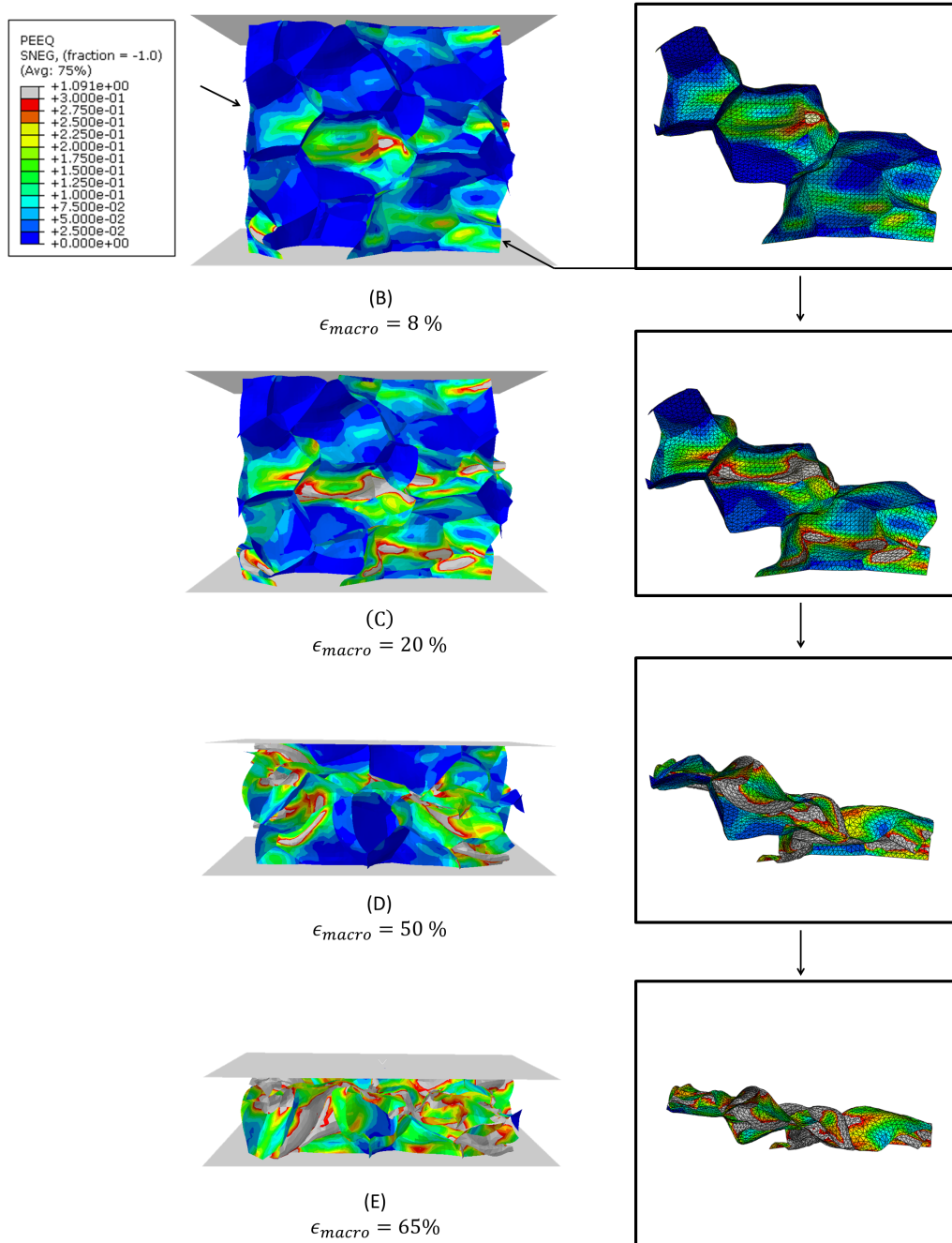


Figure 27: Distribution of equivalent plastic strain in the foam and for cells in the weak zone at points B-E of macroscopic response reported in Fig 25 (maximum of the plastic strain scale is set to 0.3 for the plot).

series of cells located in the weak zones collapse and their walls contact subsequently, which makes the macro stress oscillate. It is verified that this oscillation is attributed to the cell wall collapses and not the dynamic effect by keeping the ratio of kinetic energy to internal energy below 5%. It is noted that introducing a lower friction in the contact as well as increasing the number of cells (decreasing the cell sizes) in the model would decrease the amplitude of these oscillations. Finally, point E, is in the region in which large strains and deflections are generalized in the foam and most of the cells collapsed.

The deformation mechanisms at cell/wall level corresponding to points A to E are now investigated. Three possible deformation mechanisms at the cell level were reported in [45]: distortion, distortion in combination with rotation and distortion in combination with shear. The cells in the shell based model were verified to follow these deformation mechanisms in the simulation. For the sake of illustration, three cells with different sizes (labeled as (i), (ii), (iii) from large to small, respectively) are selected from the RVE shown in Fig 28. It is observed that the deformation mechanisms at cell level are dependent on the presence of thick cell faces and the organization of the surrounding cells. Generally, a cell with strong support (thick cell face or small neighbouring cell with thick cell faces) experience distortion combined with rotation.

At the scale of cell walls, cell failure initiates from the weakest part of the cell faces. The cell collapse then continues with buckling, bending and formation of yield lines (plastic hinges). The deformed cell faces rotate around the plastic hinges ultimately leading to self-contact/contact. This is illustrated for cell (i) by taking snapshots at three different strain points (B, C and D), as shown in Fig 29. This central large cell absorbs energy by developing plasticity in many of its faces. It is noted that the first contact in the RVE takes place in this cell at strain point C with $\epsilon_{macro} = 20\%$ (Fig 29). The ultimately contacting cell faces initially aligned with the direction of loading, carry the load and subsequently undergo plastic deformation during buckling. The formation of a yield line in the middle of the face then results in the rotation of the cell face around the yield line and self contact after collapse.

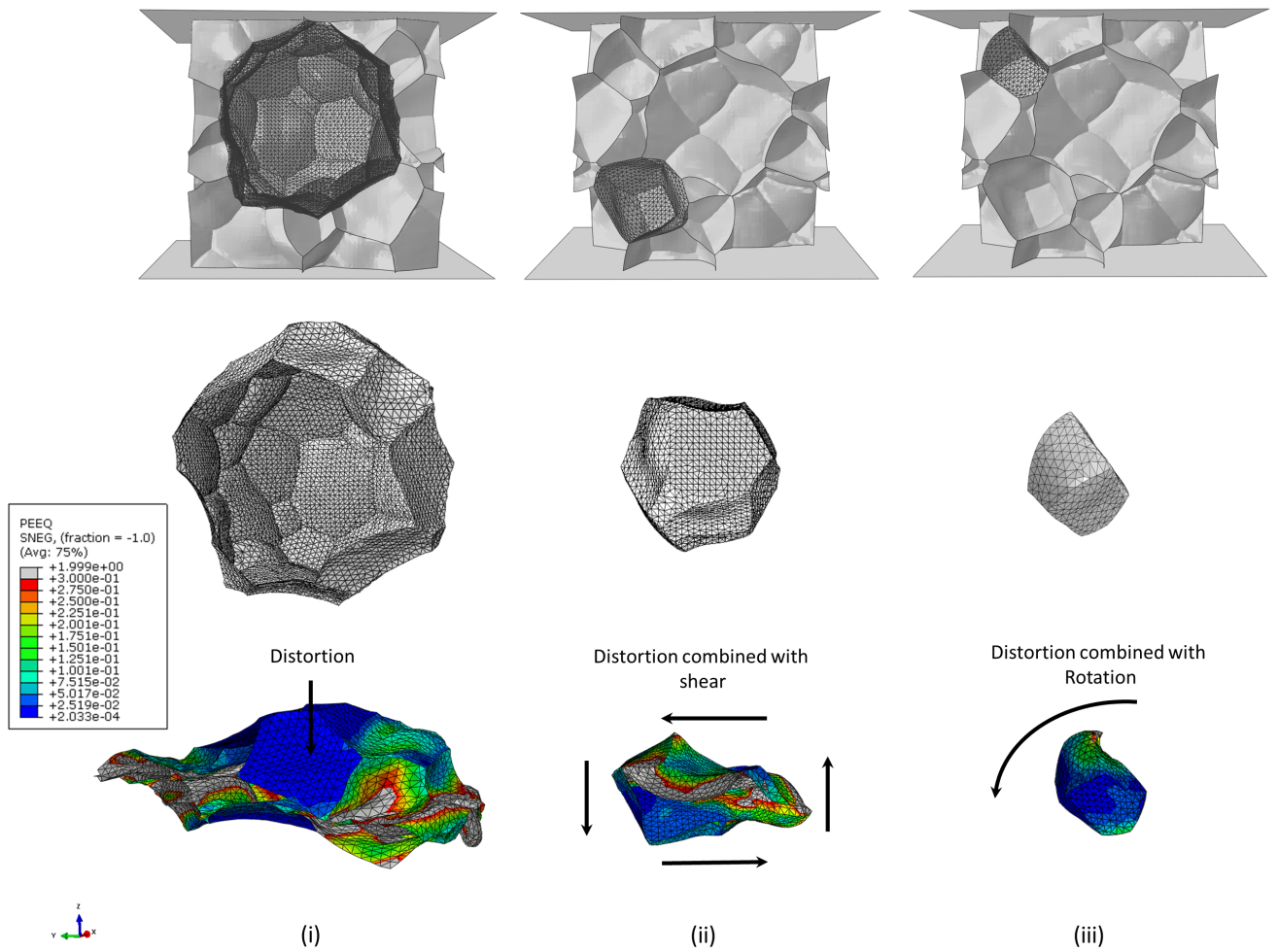


Figure 28: Three possible deformation mechanisms reported in [45] reproduced computationally in the simulation for three cells with different sizes (labeled as large (i), medium (ii) and small cell (iii)) in undeformed (top) and deformed configuration (bottom) at point D (maximum of the plastic strain scale is set to 0.3).

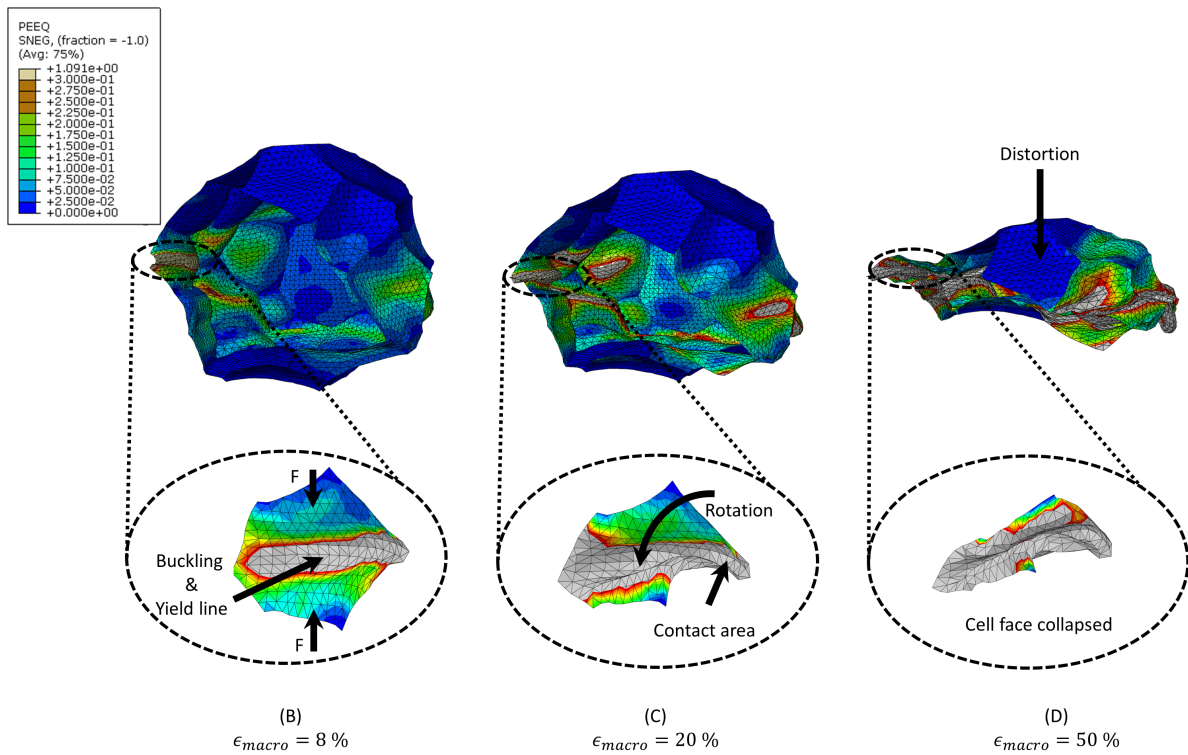


Figure 29: Distribution of equivalent plastic strain for the central large cell and one of its cell faces at points B-D of their overall response in Fig 25 (maximum of the plastic strain scale is set to 0.3).

6. Conclusion

A level set-based surface geometry extraction methodology was established to automatically generate shell finite element models of closed cell RVEs, based on a morphologically controlled 3D geometry. The closed cell foam behaviour was then investigated using shell-based modelling. A parametric study was performed to assess the individual effect of the morphological indicators on the mechanical response of closed cell metallic foams. It was observed that the findings were matching results from full 3D models.

The accuracy and efficiency of the shell-based finite element models were assessed in comparison with 3D models. The shell-based modeling could predict the macroscopic mechanical response of closed cell foams with a reasonably good accuracy at a significantly lower computational cost (a time reduction factor of 300 was obtained). The shell-based finite element models were shown to underestimate the Young modulus and overestimate the plateau stress level in comparison with the 3D models. Some sources of the errors were identified and possible solutions to decrease such errors were discussed. The shell-based model structural deformation was then investigated and compared with that of the 3D model. It was observed that shell modeling complies with the 3D modelling deformation with a reasonably good accuracy.

Due to the ability of shell modeling strategy to consider the cell wall contacts at an affordable computational cost, a foam compression study was conducted up to densification (65% macroscopic strain). The performance of the shell-based finite element modelling for predicting the macroscopic behaviour of a closed cell foam was assessed by comparing its results to experimental data from the literature. A fair agreement between shell-based finite element model and the experimental response was observed. The deformation and failure mechanisms at wall and cell levels and their link with the macroscopic behaviour of foams were investigated and trends similar to experimental observations were found.

The deformation occurs in weak zones of the foam consisting of weak cell walls. At the cell level, the larger and thinner walls which are aligned with the loading direction are the ones that deform earlier. The position of thick walls (strong support) and the organization of the neighbouring cells influence the cell deformation mechanisms. Cell wall buckling, bending and formation of yield lines were found as the collapse modes of the cell walls. It was observed that initially most of the walls buckled elastically, followed by the formation of plastic zones and yield lines; with finally deformed cells collapse and cell faces in contact.

It would be useful in a future work to extend the developed methodology to directly incorporate explicit experimental geometrical information into the computational modelling of closed cell foams. As a complement to the computational tools developed so far, 3D/shell finite element models can be built using the cell structures obtained directly from CT imaging techniques in order to capture the actual microscale geometry, see [54]. This is planned for

closed cell metallic foams as future work.

Acknowledgments

The first author acknowledge the financial support given by the Erasmus Mundus Joint Doctorate SEED project (European Commission, 2013-1436/001-001-EMJD). The work of Carlos Tiago is part of the research activity carried out at Civil Engineering Research and Innovation for Sustainability (CERIS) and has been partially financed by Fundação para a Ciência e a Tecnologia (FCT) in the framework of project UID/ECI/04625/2019.

References

- [1] A. Simone, L. Gibson, *The effects of cell face curvature and corrugations on the stiffness and strength of metallic foams*, *Acta Materialia* 46 (11) (1998) 3929–3935. doi:[https://doi.org/10.1016/S1359-6454\(98\)00072-X](https://doi.org/10.1016/S1359-6454(98)00072-X).
URL <http://www.sciencedirect.com/science/article/pii/S135964549800072X>
- [2] H. Yu, Z. Guo, B. Li, G. Yao, H. Luo, Y. Liu, *Research into the effect of cell diameter of aluminum foam on its compressive and energy absorption properties*, *Materials Science and Engineering: A* 454–455 (2007) 542–546. doi:<https://doi.org/10.1016/j.msea.2006.11.091>.
URL <http://www.sciencedirect.com/science/article/pii/S0921509306024920>
- [3] J. Yuan, Y. Li, *Effects of cell wall property on compressive performance of aluminum foams*, *Transactions of Nonferrous Metals Society of China* 25 (5) (2015) 1619 – 1625. doi:[https://doi.org/10.1016/S1003-6326\(15\)63766-9](https://doi.org/10.1016/S1003-6326(15)63766-9).
URL <http://www.sciencedirect.com/science/article/pii/S1003632615637669>
- [4] V. Deshpande, N. Fleck, *Isotropic constitutive models for metallic foams*, *Journal of the Mechanics and Physics of Solids* 48 (6) (2000) 1253–1283. doi:[https://doi.org/10.1016/S0022-5096\(99\)00082-4](https://doi.org/10.1016/S0022-5096(99)00082-4).
URL <http://www.sciencedirect.com/science/article/pii/S0022509699000824>
- [5] R. E. Raj, B. Daniel, *Customization of closed-cell aluminum foam properties using design of experiments*, *Materials Science and Engineering: A* 528 (4) (2011) 2067–2075. doi:<https://doi.org/10.1016/j.msea.2010.11.035>.
URL <http://www.sciencedirect.com/science/article/pii/S0921509310013225>
- [6] A. Markaki, T. Clyne, *The effect of cell wall microstructure on the deformation and fracture of aluminium-based foams*, *Acta Materialia* 49 (9) (2001) 1677–1686. doi:[https://doi.org/10.1016/S1359-6454\(01\)00072-6](https://doi.org/10.1016/S1359-6454(01)00072-6).
URL <http://www.sciencedirect.com/science/article/pii/S1359645401000726>
- [7] M. Islam, M. Kader, P. Hazell, A. Brown, M. Saadatfar, M. Quadir, J. Escobedo, *Investigation of microstructural and mechanical properties of cell walls of closed-cell aluminium alloy foams*, *Materials Science and Engineering: A* 666 (2016) 245–256. doi:<https://doi.org/10.1016/j.msea.2016.04.046>.
URL <http://www.sciencedirect.com/science/article/pii/S0921509316304300>
- [8] W.-Y. Jang, W.-Y. Hsieh, C.-C. Miao, Y.-C. Yen, *Microstructure and mechanical properties of ALPORAS closed-cell aluminium foam*, *Materials Characterization* 107 (2015) 228–238. doi:<https://doi.org/10.1016/j.matchar.2015.07.012>.
URL <http://www.sciencedirect.com/science/article/pii/S1044580315002594>
- [9] I. Jeon, T. Asahina, *The effect of structural defects on the compressive behavior of closed-cell Al foam*, *Acta Materialia* 53 (12) (2005) 3415–3423. doi:<https://doi.org/10.1016/j.actamat.2005.04.010>.
URL <http://www.sciencedirect.com/science/article/pii/S1359645405002089>
- [10] E. Andrews, W. Sanders, L. Gibson, *Compressive and tensile behaviour of aluminum foams*, *Materials Science and Engineering: A* 270 (2) (1999) 113–124. doi:[https://doi.org/10.1016/S0921-5093\(99\)00170-7](https://doi.org/10.1016/S0921-5093(99)00170-7).
URL <http://www.sciencedirect.com/science/article/pii/S0921509399001707>
- [11] S. A. McDonald, P. M. Mummery, G. Johnson, P. J. Withers, *Characterization of the three-dimensional structure of a metallic foam during compressive deformation*, *Journal of Microscopy* 223 (2) (2006) 150–158. doi:[10.1111/j.1365-2818.2006.01607.x](https://doi.org/10.1111/j.1365-2818.2006.01607.x).
- [12] M. Kader, M. Islam, M. Saadatfar, P. Hazell, A. Brown, S. Ahmed, J. Escobedo, *Macro and micro collapse mechanisms of closed-cell aluminium foams during quasi-static compression*, *Materials & Design* 118 (2017) 11–21. doi:<https://doi.org/10.1016/j.matdes.2017.01.011>.
URL <http://www.sciencedirect.com/science/article/pii/S0264127517300114>

- [13] H. Zhu, J. Knott, N. Mills, *Analysis of the elastic properties of open-cell foams with tetrakaidecahedral cells*, *Journal of the Mechanics and Physics of Solids* 45 (3) (1997) 319–343. doi:[https://doi.org/10.1016/S0022-5096\(96\)00090-7](https://doi.org/10.1016/S0022-5096(96)00090-7).
URL <http://www.sciencedirect.com/science/article/pii/S0022509696000907>
- [14] J. Kadkhodapour, S. Raeisi, *Micro–macro investigation of deformation and failure in closed-cell aluminum foams*, *Computational Materials Science* 83 (2014) 137–148. doi:<https://doi.org/10.1016/j.commatsci.2013.10.017>.
URL <http://www.sciencedirect.com/science/article/pii/S0927025613006344>
- [15] S. Nammi, P. Myler, G. Edwards, *Finite element analysis of closed-cell aluminium foam under quasi-static loading*, *Materials & Design* 31 (2) (2010) 712–722. doi:<https://doi.org/10.1016/j.matdes.2009.08.010>.
URL <http://www.sciencedirect.com/science/article/pii/S0261306909004312>
- [16] A. Czekanski, M. Attia, S. Meguid, M. Elbestawi, *On the use of a new cell to model geometric asymmetry of metallic foams*, *Finite Elements in Analysis and Design* 41 (13) (2005) 1327–1340. doi:<https://doi.org/10.1016/j.finel.2004.12.012>.
URL <http://www.sciencedirect.com/science/article/pii/S0168874X05000466>
- [17] J. L. Grenestedt, F. Bassinet, *Influence of cell wall thickness variations on elastic stiffness of closed-cell cellular solids*, *International Journal of Mechanical Sciences* 42 (7) (2000) 1327 – 1338. doi:[https://doi.org/10.1016/S0020-7403\(99\)00054-5](https://doi.org/10.1016/S0020-7403(99)00054-5).
URL <http://www.sciencedirect.com/science/article/pii/S0020740399000545>
- [18] C. Liu, Y. Zhang, C. Yang, *Numerical modelling of mechanical behaviour of aluminium foam using a representative volume element method*, *International Journal of Mechanical Sciences* 118 (2016) 155 – 165. doi:<https://doi.org/10.1016/j.ijmecsci.2016.08.021>.
URL <http://www.sciencedirect.com/science/article/pii/S0020740316301989>
- [19] I. Jeon, T. Asahina, K.-J. Kang, S. Im, T. J. Lu, *Finite element simulation of the plastic collapse of closed-cell aluminum foams with X-ray computed tomography*, *Mechanics of Materials* 42 (3) (2010) 227–236. doi:<https://doi.org/10.1016/j.mechmat.2010.01.003>.
URL <http://www.sciencedirect.com/science/article/pii/S0167663610000104>
- [20] O. Caty, E. Maire, S. Youssef, R. Bouchet, *Modeling the properties of closed-cell cellular materials from tomography images using finite shell elements*, *Acta Materialia* 56 (19) (2008) 5524–5534. doi:<https://doi.org/10.1016/j.actamat.2008.07.023>.
URL <http://www.sciencedirect.com/science/article/pii/S1359645408005235>
- [21] B.-Y. Su, C.-M. Huang, H. Sheng, W.-Y. Jang, *The effect of cell-size dispersity on the mechanical properties of closed-cell aluminum foam*, *Materials Characterization* 135 (2018) 203 – 213. doi:<https://doi.org/10.1016/j.matchar.2017.11.035>.
URL <http://www.sciencedirect.com/science/article/pii/S1044580317311294>
- [22] H. Zhu, P. Zhang, D. Balint, S. Thorpe, J. Elliott, A. Windle, J. Lin, *The effects of regularity on the geometrical properties of Voronoi tessellations*, *Physica A: Statistical Mechanics and its Applications* 406 (2014) 42–58. doi:<https://doi.org/10.1016/j.physa.2014.03.012>.
URL <http://www.sciencedirect.com/science/article/pii/S0378437114002064>
- [23] A. Roberts, E. Garboczi, *Elastic moduli of model random three-dimensional closed-cell cellular solids*, *Acta Materialia* 49 (2) (2001) 189–197. doi:[https://doi.org/10.1016/S1359-6454\(00\)00314-1](https://doi.org/10.1016/S1359-6454(00)00314-1).
URL <http://www.sciencedirect.com/science/article/pii/S1359645400003141>
- [24] Y. Song, Z. Wang, L. Zhao, J. Luo, *Dynamic crushing behavior of 3D closed-cell foams based on Voronoi random model*, *Materials & Design* 31 (9) (2010) 4281–4289. doi:<https://doi.org/10.1016/j.matdes.2010.04.007>.
URL <http://www.sciencedirect.com/science/article/pii/S0261306910002189>
- [25] C. Redenbach, *Microstructure models for cellular materials*, *Computational Materials Science* 44 (4) (2009) 1397–1407. doi:<https://doi.org/10.1016/j.commatsci.2008.09.018>.

- URL <http://www.sciencedirect.com/science/article/pii/S0927025608004266>
- [26] Y. Chen, R. Das, M. Battley, *Effects of cell size and cell wall thickness variations on the stiffness of closed-cell foams*, *International Journal of Solids and Structures* 52 (2015) 150–164. doi:<https://doi.org/10.1016/j.ijsolstr.2014.09.022>.
URL <http://www.sciencedirect.com/science/article/pii/S0020768314003692>
- [27] C. Redenbach, I. Shklyar, H. Andr, *Laguerre tessellations for elastic stiffness simulations of closed foams with strongly varying cell sizes*, *International Journal of Engineering Science* 50 (1) (2012) 70–78. doi:<https://doi.org/10.1016/j.ijengsci.2011.09.002>.
URL <http://www.sciencedirect.com/science/article/pii/S0020722511001807>
- [28] X. Shi, S. Liu, H. Nie, G. Lu, Y. Li, *Study of cell irregularity effects on the compression of closed-cell foams*, *International Journal of Mechanical Sciences* 135 (2018) 215 – 225. doi:<https://doi.org/10.1016/j.ijmecsci.2017.11.026>.
URL <http://www.sciencedirect.com/science/article/pii/S0020740317322890>
- [29] Y. Zhang, T. Jin, S. Li, D. Ruan, Z. Wang, G. Lu, *Sample size effect on the mechanical behavior of aluminum foam*, *International Journal of Mechanical Sciences* 151 (2019) 622 – 638. doi:<https://doi.org/10.1016/j.ijmecsci.2018.12.019>.
URL <http://www.sciencedirect.com/science/article/pii/S0020740318328297>
- [30] Z. Zheng, Y. Liu, J. Yu, S. R. Reid, *Dynamic crushing of cellular materials: Continuum-based wave models for the transitional and shock modes*, *International Journal of Impact Engineering* 42 (2012) 66–79. doi:<https://doi.org/10.1016/j.ijimpeng.2011.09.009>.
URL <http://www.sciencedirect.com/science/article/pii/S0734743X11001497>
- [31] A. Ghazi, P. Berke, K. E. M. Kamel, B. Sonon, C. Tiago, T. Massart, *Multiscale computational modelling of closed cell metallic foams with detailed microstructural morphological control*, *International Journal of Engineering Science* 143 (2019) 92 – 114. doi:<https://doi.org/10.1016/j.ijengsci.2019.06.012>.
URL <http://www.sciencedirect.com/science/article/pii/S0020722519300631>
- [32] B. Sonon, B. François, T. J. Massart, *An advanced approach for the generation of complex cellular material representative volume elements using distance fields and level sets*, *Computational Mechanics* 56 (2) (2015) 221–242. doi:[10.1007/s00466-015-1168-8](https://doi.org/10.1007/s00466-015-1168-8).
URL <https://doi.org/10.1007/s00466-015-1168-8>
- [33] N. Kilingar, K. E. M. Kamel, B. Sonon, T. Massart, L. Noels, *Computational generation of open-foam representative volume elements with morphological control using distance fields*, *European Journal of Mechanics - A/Solids* 78 (2019) 103847. doi:<https://doi.org/10.1016/j.euromechsol.2019.103847>.
URL <http://www.sciencedirect.com/science/article/pii/S0997753818308854>
- [34] B. Sonon, B. François, T. J. Massart, *A unified level set based methodology for fast generation of complex microstructural multi-phase RVEs*, *Computer Methods in Applied Mechanics and Engineering* 223-224 (2012) 103–122. doi:<https://doi.org/10.1016/j.cma.2012.02.018>.
URL <http://www.sciencedirect.com/science/article/pii/S0045782512000606>
- [35] K. Ehab Moustafa Kamel, B. Sonon, T. J. Massart, *An integrated approach for the conformal discretization of complex inclusion-based microstructures*, *Computational Mechanics* doi:[10.1007/s00466-019-01693-4](https://doi.org/10.1007/s00466-019-01693-4).
URL <https://doi.org/10.1007/s00466-019-01693-4>
- [36] B. Wintiba, B. Sonon, K. E. M. Kamel, T. J. Massart, *An automated procedure for the generation and conformal discretization of 3d woven composites rves*, *Composite Structures* 180 (2017) 955 – 971. doi:<https://doi.org/10.1016/j.compstruct.2017.08.010>.
URL <http://www.sciencedirect.com/science/article/pii/S0263822317319190>
- [37] T. Miyoshi, *ALPORAS aluminum foam: production process, properties, and applications*, *Advanced engineering materials* 2 (4) (2000) 179–183. doi:[10.1002/\(SICI\)1527-2648\(200004\)2:4<179::AID-ADEM179>3.0.CO;2-G](https://doi.org/10.1002/(SICI)1527-2648(200004)2:4<179::AID-ADEM179>3.0.CO;2-G).

- [38] W. E. Lorensen, H. E. Cline, [Marching cubes: A high resolution 3d surface construction algorithm](#), SIGGRAPH Comput. Graph. 21 (4) (1987) 163–169. doi:[10.1145/37402.37422](https://doi.org/10.1145/37402.37422).
URL <http://doi.acm.org/10.1145/37402.37422>
- [39] M. Kazhdan, M. Bolitho, H. Hoppe, Poisson surface reconstruction, Eurographics Symposium on Geometry Processing.
- [40] L. D. Angelo, P. D. Stefano, L. Giaccari, [A new mesh-growing algorithm for fast surface reconstruction](#), Computer-Aided Design 43 (6) (2011) 639 – 650. doi:<https://doi.org/10.1016/j.cad.2011.02.012>.
URL <http://www.sciencedirect.com/science/article/pii/S0010448511000571>
- [41] F. Bernardini, J. Mittleman, H. Rushmeier, C. Silva, G. Taubin, The ball-pivoting algorithm for surface reconstruction, IEEE transactions on visualization and computer graphics 5(4) (1999) 349–359.
- [42] P. Cignoni, M. Callieri, M. Corsini, M. Dellepiane, F. Ganovelli, G. Ranzuglia, Meshlab: an open-source mesh processing tool, Sixth Eurographics Italian Chapter Conference (2008) 129 – 136.
- [43] H. Si, [Tetgen, a delaunay-based quality tetrahedral mesh generator](#), ACM Trans. Math. Softw. 41 (2) (2015) 11:1–11:36. doi:[10.1145/2629697](https://doi.org/10.1145/2629697).
URL <http://doi.acm.org/10.1145/2629697>
- [44] Simulia, Abaqus 6.14 – Analysis User’s Manual, Dassault systèmes., 2014.
- [45] Y. Mu, G. Yao, L. Liang, H. Luo, G. Zu, [Deformation mechanisms of closed-cell aluminum foam in compression](#), Scripta Materialia 63 (6) (2010) 629–632. doi:<https://doi.org/10.1016/j.scriptamat.2010.05.041>.
URL <http://www.sciencedirect.com/science/article/pii/S1359646210003660>
- [46] V. Kouznetsova, W. A. M. Brekelmans, F. P. T. Baaijens, [An approach to micro-macro modeling of heterogeneous materials](#), Computational Mechanics 27 (1) (2001) 37–48. doi:[10.1007/s004660000212](https://doi.org/10.1007/s004660000212).
URL <https://doi.org/10.1007/s004660000212>
- [47] W. Tian, L. Qi, X. Chao, J. Liang, M. Fu, [Periodic boundary condition and its numerical implementation algorithm for the evaluation of effective mechanical properties of the composites with complicated micro-structures](#), Composites Part B: Engineering 162 (2019) 1 – 10. doi:<https://doi.org/10.1016/j.compositesb.2018.10.053>.
URL <http://www.sciencedirect.com/science/article/pii/S1359836818319838>
- [48] B. C. N. Mercatoris, T. J. Massart, Assessment of periodic homogenization-based multiscale computational schemes for quasi-brittle structural failure, International Journal for Multiscale Computational Engineering 7 (2) (2009) 153–170.
- [49] M. A. Hasan, An improved model for fe modeling and simulation of closed cell al-alloy foams, Advances in Materials Science and Engineering doi:<http://dx.doi.org/10.1155/2010/567390>.
- [50] I. Jeon, K. Katou, T. Sonoda, T. Asahina, K.-J. Kang, [Cell wall mechanical properties of closed-cell Al foam](#), Mechanics of Materials 41 (1) (2009) 60–73. doi:<https://doi.org/10.1016/j.mechmat.2008.08.002>.
URL <http://www.sciencedirect.com/science/article/pii/S0167663608001087>
- [51] Y. Sun, B. Amirrasouli, S. Razavi, Q. Li, T. Lowe, P. Withers, [The variation in elastic modulus throughout the compression of foam materials](#), Acta Materialia 110 (2016) 161–174. doi:<https://doi.org/10.1016/j.actamat.2016.03.003>.
URL <http://www.sciencedirect.com/science/article/pii/S1359645416301446>
- [52] Y. Sun, Q. Li, T. Lowe, S. McDonald, P. Withers, [Investigation of strain-rate effect on the compressive behaviour of closed-cell aluminium foam by 3d image-based modelling](#), Materials & Design 89 (2016) 215 – 224. doi:<https://doi.org/10.1016/j.matdes.2015.09.109>.
URL <http://www.sciencedirect.com/science/article/pii/S0264127515305190>

- [53] Y. Chen, R. Das, M. Battley, *Effects of cell size and cell wall thickness variations on the strength of closed-cell foams*, International Journal of Engineering Science 120 (2017) 220–240. doi:<https://doi.org/10.1016/j.ijengsci.2017.08.006>.
URL <http://www.sciencedirect.com/science/article/pii/S0020722516314318>
- [54] K. Ehab Moustafa Kamel, J.-B. Colliat, P. Gerard, T. J. Massart, *Comparison of advanced discretization techniques for image-based modelling of heterogeneous porous rocks*, Acta Geotechnica doi:10.1007/s11440-019-00798-7.
URL <https://doi.org/10.1007/s11440-019-00798-7>